










Joint *HST*, *VLT/MUSE*, and *XMM–Newton* observations to constrain the mass distribution of the two strong lensing galaxy clusters: MACS J0242.5-2132 and MACS J0949.8+1708

Joseph F. V. Allingham ¹★, Mathilde Jauzac ^{2,3,4,5}, David J. Lagattuta ^{2,3}, Guillaume Mahler ^{2,3}, Céline Bøhm ¹, Geraint F. Lewis ¹, Dominique Eckert ⁶, Alastair Edge ² and Stefano Ettori ^{7,8}

¹*School of Physics, A28, The University of Sydney, New South Wales 2006, Australia*

²*Centre for Extragalactic Astronomy, Department of Physics, Durham University, South Road, Durham DH1 3LE, UK*

³*Institute for Computational Cosmology, Department of Physics, Durham University, South Road, Durham DH1 3LE, UK*

⁴*Astrophysics Research Centre, University of KwaZulu-Natal, Westville Campus, Durban 4041, South Africa*

⁵*School of Mathematics, Statistics & Computer Science, University of KwaZulu-Natal, Westville Campus, Durban 4041, South Africa*

⁶*Department of Astronomy, University of Geneva, ch. d'Écogia 16, Versoix CH-1290, Switzerland*

⁷*INAF - Osservatorio di Astrofisica e Scienza dello Spazio di Bologna, via Piero Gobetti 93/3, Bologna 40129, Italy*

⁸*INFN, Sezione di Bologna, viale Berti Pichat 6/2, Bologna 40127, Italia*

Accepted 2023 March 3. Received 2023 January 31; in original form 2022 July 20

ABSTRACT

We present the strong lensing analysis of two galaxy clusters: MACS J0242.5-2132 (MACS J0242, $z = 0.313$) and MACS J0949.8+1708 (MACS J0949, $z = 0.383$). Their total matter distributions are constrained, thanks to the powerful combination of observations with the *Hubble Space Telescope* (*HST*) and the Multi-Unit Spectroscopic Explorer instrument. Using these observations, we precisely measure the redshift of six multiple image systems in MACS J0242 and two in MACS J0949. We also include four multiple image systems in the latter cluster identified in *HST* imaging without MUSE redshift measurements. For each cluster, our best-fit mass model consists of a single cluster-scale halo and 57 (170) galaxy-scale halos for MACS J0242 (MACS J0949). Multiple images positions are predicted with a rms 0.39 arcsec and 0.15 arcsec for MACS J0242 and MACS J0949 models, respectively. From these mass models, we derive aperture masses of $M(R < 200 \text{ kpc}) = 1.67_{-0.05}^{+0.03} \times 10^{14} M_{\odot}$ and $M(R < 200 \text{ kpc}) = 2.00_{-0.20}^{+0.05} \times 10^{14} M_{\odot}$. Combining our analysis with X-ray observations from the *XMM–Newton Observatory*, we show that MACS J0242 appears to be a relatively relaxed cluster, whereas conversely, MACS J0949 shows a relaxing post-merger state. At 200 kpc, X-ray observations suggest the hot gas fraction to be, respectively, $f_g = 0.115_{-0.004}^{+0.003}$ and $0.053_{-0.006}^{+0.007}$ for MACS J0242 and MACS J0949. MACS J0242 being relaxed, its density profile is very well fitted by a Navarro–Frenk–White distribution, in agreement with X-ray observations. Finally, the strong lensing analysis of MACS J0949 suggests a flat dark matter density distribution in the core, between 10 and 100 kpc. This appears consistent with X-ray observations.

Key words: cosmology: observations – cosmology: dark matter – gravitational lensing: strong – galaxies: clusters: general.

1 INTRODUCTION

One of the most promising avenues towards understanding the nature of dark matter is to study its gravitational influence on the universe’s large-scale structure, particularly within the most massive galaxy clusters. These gravitationally bound clusters act as the largest natural laboratories, allowing not only to observe the large-scale baryonic physics, but also to indirectly probe dark matter thanks to the effect of gravitational lensing. Gravitational lensing is the phenomenon of optical distortion of background images, occurring when a massive foreground object – like a cluster, the ‘lens’ – is on its line-of-sight. Gravitational lenses act as magnifying telescopes of objects in the background, creating in some cases multiple images of a same source,

and allowing observers to study objects in the distant universe (for a review, see Kneib & Natarajan 2011).

For all these reasons, since the first discovery of the gravitational giant arc of Abell 370 (Hammer 1987; Soucail et al. 1988) to the modern surveys of galaxy clusters and gravitational lenses, such as the Cluster Lensing And Supernovae survey with Hubble (CLASH, Postman et al. 2012), the Hubble Frontier Fields (HFF, PI: Lotz, Lotz et al. 2017), the REionization Lensing Cluster Survey (RELICS, PI: Coe, Coe et al. 2019), the SDSS Giant Arcs Survey (SGAS, PI: Gladders, Sharon et al. 2020), and the Beyond the Ultra-deep Frontier Fields And Legacy Observation programme (BUFFALO, PI: Steinhardt & Jauzac, Steinhardt et al. 2020), gravitational lensing has emerged as a field of cosmology, capable of bringing key information to comprehend the structure formation and the nature of dark matter.

In particular, the study of a system of multiple images originating from one source through gravitational lensing allows one to constrain

* E-mail: jall0809@uni.sydney.edu.au

the mass distribution within the lens and to characterize the dark matter density profile within it. The descriptive potential of gravitational lensing has already been showcased at multiple occasions, such as in Jauzac et al. 2014; Richard et al. 2014a; Grillo et al. 2015; Diego et al. 2015a, b, 2016; Jauzac et al. 2016c; Caminha et al. 2017; Diego et al. 2018; Williams, Sebesta & Liesenborgs 2018; Diego et al. 2020. Using the combination of high-resolution images taken with the *Hubble Space Telescope* (*HST*) and the Dark Energy Survey (DES) for photometric analysis in the one hand, and the Multi-Unit Spectroscopic Explorer (MUSE, see Bacon et al. 2014) for spectroscopy in the other, we were able to securely identify cluster members and multiple images systems. This combination has proven to be particularly successful over the past few years (e.g. Grillo et al. 2016; Treu et al. 2016; Jauzac et al. 2016a; Lagattuta et al. 2017; Mahler et al. 2017; Caminha et al. 2019; Jauzac et al. 2019; Lagattuta et al. 2019; Jauzac et al. 2021).

In this paper, we repeat a similar exercise, looking at two galaxy clusters, MACS J0242.5–2132 and MACS J0949.8+1708 (i.e. RXC J0949.8+1707), hereafter MACS J0242 and MACS J0949 respectively, initially discovered by the MAssive Cluster Survey (MACS, PI: Ebeling, Ebeling, Edge & Henry 2001). We combined multiband *HST* and ground-based imaging with spectroscopy from VLT/MUSE with the lensing modelling technique presented in detail in Richard et al. (2014b) which makes use of the publicly available LENSTOOL software (Kneib et al. 1996; Jullo et al. 2007). We then confront our lensing results to the intra-cluster gas distribution observed by the *XMM–Newton* X-ray Observatory.

It is common practice to use the combined baryonic analysis of the X-ray signal and the Sunyaev-Zel’dovich effect (SZ) to understand the thermodynamics of galaxy clusters. One can then reconstruct the total matter density of galaxy clusters by making a number of hypotheses, such as hydrostatic equilibrium or polytropic temperature distribution (see Tchernin et al. 2018). Furthermore, as the analysis of multiwavelength observations (optical, SZ effect, X-rays) characterizes the thermodynamics of the intra-cluster medium (ICM; see Sereno et al. 2017), a careful comparison between these and a strong lensing analysis can provide clues on the possible differences between expected and observed baryon and dark matter distributions.

As an example, the study in merging galaxy clusters of the offset between the position of the centre of dark matter, luminous galaxies, and X-ray emission can be used to constrain the cross-section of self-interacting dark matter (SIDM, see Tulin & Yu 2018, for an overview). In fact, simulations of colliding clusters suggests the cold dark matter (CDM) distribution to be bounded to the luminous distribution; whereas in SIDM scenarios dark matter lags behind baryonic matter (Massey, Kitching & Nagai 2011; Robertson, Massey & Eke 2016, 2017). For instance, Robertson, Massey & Eke (2017) present SIDM simulations with anisotropic scattering, yielding an offset between the galaxies centre and that of dark matter (DM) smaller than 10 kpc for an interaction $\sigma/m = 1 \text{ cm}^2 \cdot \text{g}^{-1}$. This was pioneered in Clowe, Gonzalez & Markevitch (2004) and Bradač et al. (2008) and has now become more and more popular as shown in, e.g. Merten et al. (2011); Harvey et al. (2015); Massey et al. (2015); Jauzac et al. (2016b); Jauzac, Harvey & Massey (2018); Massey et al. (2018).

In this article, we focus on the lensing-based mass reconstructions of the two clusters. Utilizing the ICM detected in the X-rays to infer the dark matter halo profile, we compare the results of our lensing reconstruction to the *XMM–Newton* X-ray data from CHEX-MATE Collaboration et al. (2021), processed following the X-COP pipeline (Ghirardini et al. 2019) for these two clusters. We present a broader context for such comparisons, i.e. new models of baryonic matter distribution rooted in lensing analysis to constrain the electronic

densities of galaxy clusters, in a companion paper (Allingham et al. in prep.).

Our paper is organized as follows. In Section 2, we present the observations used for our analysis. The methods to extract multiple image candidates and to build cluster galaxy catalogues are presented in Section 3. The lensing reconstruction method is introduced in Section 4, the mass models are described in Section 5, and conclusions are presented in Section 6. Throughout this paper, we assume the Λ CDM cosmological model, with $\Omega_m = 0.3$, $\Omega_\Lambda = 0.7$, and $H_0 = 70 \text{ km/s/Mpc}$. All magnitudes use the AB convention system (Oke 1974).

2 DATA

To determine the cluster mass distributions as robustly as possible, we include both imaging and spectroscopic information when constructing lens models. This combination is especially powerful, allowing us to identify and confirm individual components of the model (such as multiple-image constraints and cluster members) while simultaneously rejecting interlopers along the line of sight. We complement the observations we have with *HST* and VLT/MUSE with *XMM–Newton* X-ray Observatory observations to cross-check our lensing model results. Figures 1 and 2 present a stack of the imaging, spectroscopic, and X-ray data for clusters MACS J0242 and MACS J0949 respectively.

2.1 Imaging

2.1.1 Hubble Space Telescope

As part of the MACS survey (Ebeling et al. 2001), both targets in our study have publicly available *HST* data. Snapshot (1200s) imaging of MACS J0242 taken with the Wide Field Planetary Camera 2 (WFPC2, Holtzman et al. 1995) exists for both the F606W and F814W bands (PID:11103, PI: Ebeling), supplemented by an additional 1200s image taken with the Advanced Camera for Surveys (ACS, Ford et al. 1998) in F606W (PID: 12166, PI: Ebeling). Similarly, shallow imaging for MACS J0949 have been taken with the ACS in both F606W (PID:10491, PI: Ebeling) and F814W (PID: 12166, PI: Ebeling). Archival processed versions of these datasets are available from the *Hubble* Legacy Archive.¹

Following the initial MACS data, MACS J0949 was subsequently observed as part of the RELICS survey (Coe et al. 2019) – under the name RXC J0949.8+1707 – and thus there are additional data sets for this cluster. Specifically, ACS imaging in F435W, F606W, and F814W provide wider, deeper coverage of the cluster field in optical bands, whereas coverage in F105W, F125W, F140W, and F160W bands using the Wide Field Camera 3 (WFC3, Kalirai et al. 2009) provide information in the near-infrared regime. These data are also publicly available² and therefore in this work combine all of the imaging (save for the F435W band, which is too low S/N for our purposes) to create our master data set. A summary of all available *HST* imaging can be found in Table 1.

2.1.2 DESI legacy survey

Since the available *HST* imaging for MACS J0242 are shallow and colour information is limited to a WFPC2-sized footprint, we complement these data with additional multiband ground-based

¹<https://hla.stsci.edu/>

²<https://archive.stsci.edu/prepds/relics/>

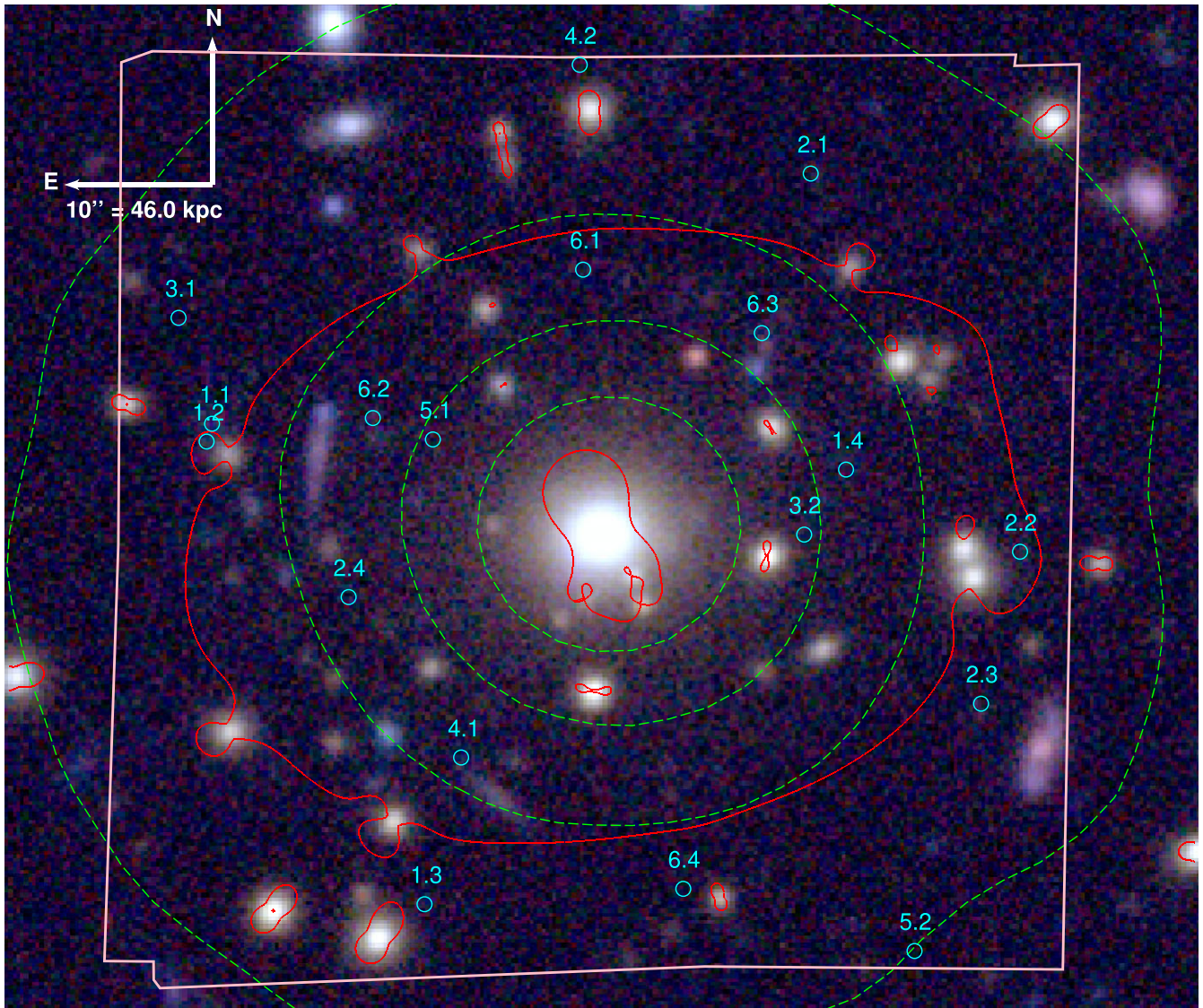


Figure 1. Composite DES colour image of MACSJ0242. The gas distribution obtained from *XMM–Newton* observations is shown with dashed green contours. In cyan, we highlight the positions of the multiple images used to constrain the mass model and which are listed in Table 6. Critical lines for a source at $z = 3.0627$ (redshift of system 1) are shown in red. The MUSE field of view is shown in pink.

imaging from the Dark Energy Spectroscopic Instrument (DESI) legacy archive. To enhance the *HST* data as much as possible, we extract cutout images in three optical bands – g, r, and z, see Abbott et al. (2018). The images are centred around the MACSJ0242 brightest cluster galaxy (BCG) located at ($\alpha = 40.6497$ deg, $\delta = -21.5406$ deg), and extend over a full ACS field of view. Combining the space- and ground-based information allow us to improve our galaxy selection function during lens modelling (see Section 3). The DESI data are summarized in Table 2.

2.2 Spectroscopy

In addition to imaging, our lensing reconstruction makes use of the MUSE (Bacon et al. 2014) observations at the very large telescope. Such observations are invaluable to obtain redshift information. Both clusters were observed with MUSE as part of the filler large programme ‘A MUSE survey of the most massive clusters of galaxies – the universe’s kleidoscopes’ (PI: Edge). Data for each cluster

consist of a single MUSE pointing, divided in a series of three exposures of 970 s. To reduce the effects of bad pixels, cosmic rays, and other systematics, each successive exposure is rotated by 90° , and a small (~ 0.05 arcsec) dither pattern is applied. We reduce the raw data following the procedure detailed in Richard et al. (2021). Details of the observations for both clusters are summarized in Table 3.

2.3 X-ray data

We searched the *XMM–Newton* archive for publicly available observations of the two systems of interest. MACSJ0242 was observed for a total of 70 ks (OBSID:0673830101) and MACSJ0949 for a total of 36 ks (OBSID:0827340901). We analysed the two observations using XMMSAS v17.0, and the most up-to-date calibration files. We used the XMMSAS tools `mos-filter` and `pn-filter` to extract light curves of the observations and filter out periods of enhanced background, induced by soft proton flares. After flare filtering, the

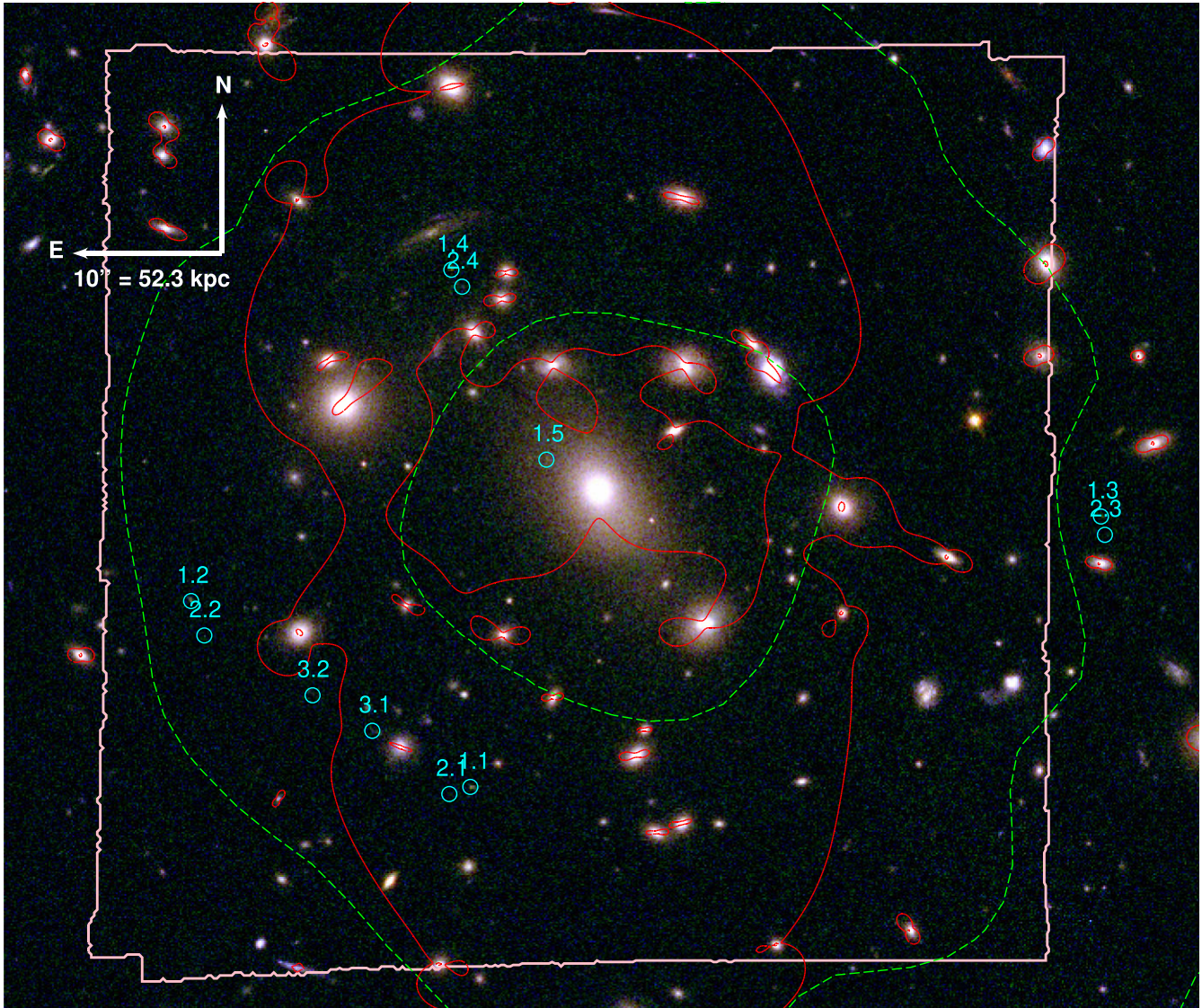


Figure 2. Composite colour *HST* image of MACS J0949. The critical lines of system 1, at redshift 4.8902, are shown in red. The gas distribution obtained thanks to *XMM–Newton* observations are shown with dash green contours. In cyan, we highlight the positions of the multiple images used to constrain the mass model. They are listed in Table 8. In pink, we display the MUSE field of view.

Table 1. Summary of the *HST* observations used in this analysis for MACS J0242 and MACS J0949.

Galaxy cluster	Date of observation	Proposal	Camera/Filter	RA (°, J2000)	Dec (°, J2000)	Exposure time (s)
MACS J0242	29/02/2012	12 166	ACS/F606W	40.645985	−21.541129	1200
	30/11/2007	11 103	WFPC2/F606W	40.649625	−21.540556	1200
	27/10/2008	11 103	WFPC2/F814W	40.649625	−21.540556	1200
MACS J0949	09/10/2015	14 096	WFC3/F105W	147.462029	17.120908	706
	09/10/2015	14 096	WFC3/F125W	147.462029	17.120908	356
	09/10/2015	14 096	WFC3/F140W	147.462029	17.120908	331
	09/10/2015	14 096	WFC3/F160W	147.462029	17.120908	906
	20/11/2015	14 096	ACS/F606W	147.463077	17.120878	1013
	20/11/2015	14 096	ACS/F814W	147.463077	17.120878	1013
	23/04/2011	14 096	ACS/F814W	147.463077	17.120878	1440
	25/10/2005	14 096	ACS/F606W	147.463077	17.120878	1200

Table 2. Summary of the DESI observations used in this analysis for MACS J0242.

Date of observation ^a	Proposal	Filter	RA (°, J2000)	Dec (°, J2000)	Exposure time (s)	Seeing (″) ^a
24/09/2016	2012B-0001	DES/g	40.6497	−21.5406	810	0.738
05/11/2016	2012B-0001	DES/r	40.6497	−21.5406	720	0.701
16/11/2016	2012B-0001	DES/z	40.6497	−21.5406	810	0.859

Note.^a Median values, determined over all observations.

Table 3. Summary of MUSE observations for MACS J0242 and MACS J0949. Columns 1 to 3 indicate respectively the name of the cluster, its average redshift, and the ID of the ESO programme. For each pointing, we then give the observation date in column 4, the right ascension, R.A., and declination, Dec., of the centre of the field of view in columns 5 and 6, the total exposure time in column 7, and the full width at half maximum (FWHM) of the seeing during the observations in column 8.

Galaxy cluster	z	Date of observation	ESO proposal	RA (°, J2000)	Dec (°, J2000)	Exposure time (s)	Seeing (″)
MACS J0242	0.3131	26/12/2017	0100.A-0792(A)	40.650167	−21.5401389	2910	0.63
MACS J0949	0.383	20/02/2020	0104.A-0801(A)	147.465792	17.119528	2910	0.71

available clean exposure time is 61 ks (MOS) and 53 ks (PN) for MACS J0242, and 35 ks (MOS) and 34 ks (PN) for MACS J0949.

3 SPECTROSCOPIC AND PHOTOMETRIC ANALYSES

In this section, we present the key steps to obtain cluster galaxy catalogues and (candidate) background multiple image systems for both MACS J0242 and MACS J0949: from the source extraction to the selections of galaxies and identification of cluster galaxies specifically, using both the multiband imaging in hand for the two clusters as well as the spectroscopy from VLT/MUSE.

3.1 Spectroscopic analysis

We here present the analysis of the spectroscopic observations described in Section 2.2. In spite of the field of view of the MUSE cubes, 1 arcmin \times 1 arcmin, being smaller than that of *HST* or DES, we can still access the redshift of a large number of foreground, cluster, and background galaxies.

In order to detect specifically multiple image systems, we use MUSELET (MUSE Line Emission Tracker), a package of MPDAF (Muse Python Data Analysis Framework) which removes the constant emission from bright galaxies in the field and is optimized for the detection of the faintest objects. For more details about the technique, we refer the reader to (Bacon et al. 2016) and (Piqueras et al. 2017). We go through each of the 3681 slices of this subtracted MUSE datacube and identify the bright detections.

We complete this technique with CatalogueBuilder (see Richard et al. 2021) for a thorough and systematic analysis. The latter embeds the MUSELET analysis, but also uses a modified version of MARZ (see Hinton et al. 2016), which is better tuned to the resolution and spectral profiles specific to MUSE data. CatalogueBuilder also uses the position data of the deepest field available (in this case *HST/ACS*). These make it easier to confirm the likely source of the multiple images which we are looking for. Using the spectroscopic information, we adjust with our own custom redshifting routine the detected spectra to the known absorption lines, and notably [OII], [OIII] and Ly- α . We then obtain catalogues containing coordinates and redshifts, such as Tables 6 and A1. We also consider multiple detections within a radius of <0.5 arcsec and a redshift separation of $\delta z < 0.05$ to be a unique object. All redshifts are supposed known with a precision estimated to $\delta z = 0.0001$.

We can associate to these detections Signal-to-Noise (S/N) ratios. As we also know the type of pattern the absorption lines should match, we can use the S/N ratio and spectral patterns to define different confidence levels. We only keep in all catalogues, including for example in Section A, detections judged to be ‘good’ or ‘excellent’ (identifiers 3 and 4 in MARZ and CatalogueBuilder). In the case of several detections representing a same object, we merge them keeping the best quality of detection.

The distribution of redshifts in each cluster is shown in Fig. 3 for the full MUSE frame. We measure 36 and 96 good spectroscopic redshifts in MACS J0242 and MACS J0949, respectively. Due to the small statistics, this distribution is not Gaussian but it is sufficient to constrain the redshift of the clusters, which we estimate to be $0.300 \leq z \leq 0.325$ and $0.36 \leq z \leq 0.41$ for MACS J0242 and MACS J0949, respectively. For the current analysis, we define the redshift of each cluster by that of their BCG, i.e. respectively 0.3131 and 0.383 for MACS J0242 and MACS J0949, respectively.

3.2 Photometric analysis

3.2.1 Source extraction

We first align all images from a given instrument (*HST/ACS*, *HST/WFC3*, *HST/WFPC2*, and DESI) to the same wcs coordinates and pixelate them accordingly to allow for direct colour comparison of detected objects. In order to extract all detected objects from the multiband imaging in hand for each cluster, we run the SEXTRACTOR software (Bertin & Arnouts 1996) in dual-image mode, for each pass-band of each instrument. For each instrument, we adopt a reference pass-band and a position of reference. The former sets the Kron-like magnitude of each detection, whereas the latter sets its location. The number of bands per instrument as well as the reference pass-band used is listed in Tables 4 and 5 for MACS J0242 and MACS J0949, respectively.

For each instrument, we then apply several cuts and selection criteria to the output catalogues from SEXTRACTOR. That allows us to build a complete multiband catalogue composed only of galaxies. We summarize the different steps of this process:

(i) All detections without reliable magnitude measurements (i.e. MAG_AUTO=−99) and incomplete (or corrupted) data are removed from all catalogues. This includes isophotal data and memory overflow that occurs during deblending or extraction.

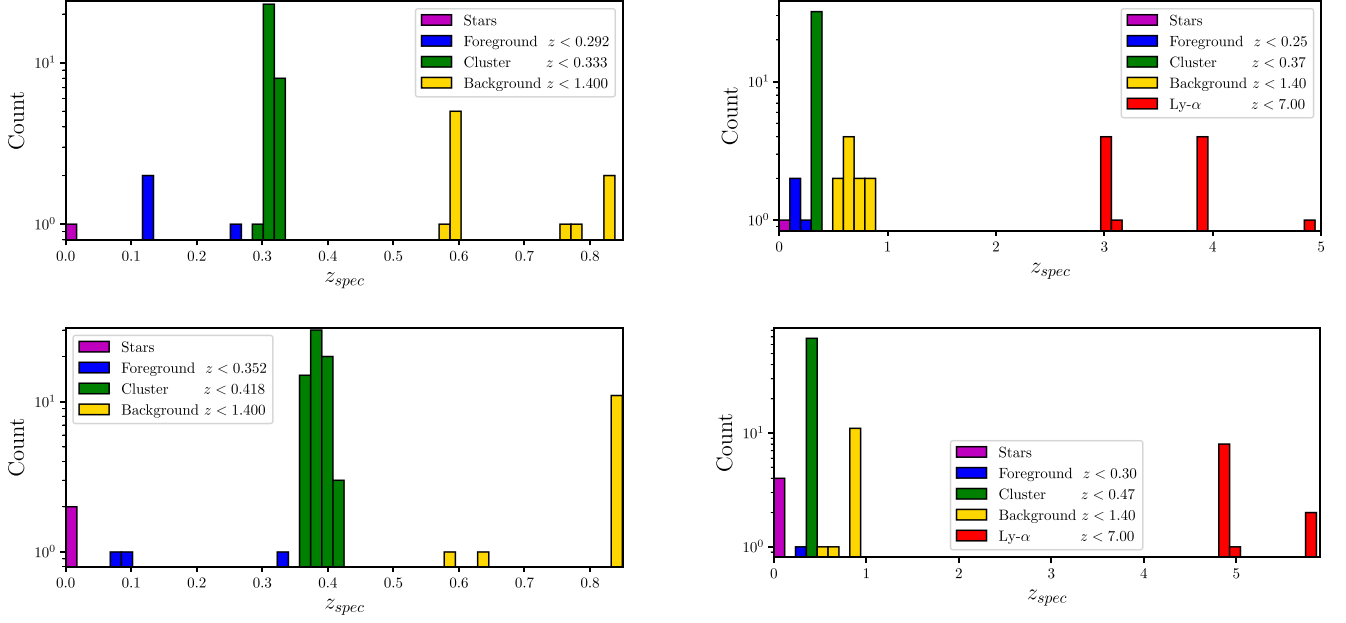


Figure 3. Redshift distribution of all MUSE detected objects. Top row: cluster MACS J0242. Objects identified as being in the cluster are shown in green, whereas foreground and background objects are shown in blue and yellow, respectively. We highlight Lyman- α emitters in red. At last, objects within the Milky Way (stars, etc.) are displayed in purple. Left panel: redshift distribution of objects located at small redshifts $z < 1$. – Right panel: redshift distribution of all objects with a measured redshift. Bottom row: cluster MACS J0949. Left panel: redshift distribution of objects located at small redshifts $z < 1$. – Right panel: redshift distribution of all objects with a measured redshift.

Table 4. Number of detections (Nod) after each source extraction selections as listed in Section 3.2.1 for MACS J0242.

Observable	DES	<i>HST</i> /WFPC2	<i>HST</i> /ACS
Number of bands	3	2	1
Reference band	z	F814W	F606W
Nod (0)	186	808	559
Nod (i)	185	540	559
Nod (ii)	180	492	456
Nod (iii)	180	429	456
Nod (iv)	142	202	402
Colour-magnitude	51	45	179
Final		58	

(ii) All objects with a stellarity greater than 0.2 are removed as they are likely to be stars rather than galaxies. We additionally mask all detections very close to bright stars.

(iii) For a given cluster, only objects detected in all pass-bands are kept.

(iv) All objects with a S/N ratio smaller than 10 are removed.

Tables 4 and 5 are listing the number of detections remaining once each of these criteria are applied for each instrument, for MACS J0242 and MACS J0949, respectively.

3.2.2 Spectroscopic redshift identification

Now that we have a galaxy catalogue for each instrument, we can match our detection with spectroscopic redshift measurements from VLT/MUSE. In order to ensure a MUSE detection corresponds to a photometric one, we compare the positions measured by SEXTRAC–

Table 5. Number of detections (Nod) after each source extraction selections as listed in Section 3.2.1 for MACS J0949.

Observable	<i>HST</i> /WFC3	<i>HST</i> /ACS
Number of bands	4	2
Reference band	F160W	F814W
Nod (0)	3114	3055
Nod (i)	2388	2700
Nod (ii)	2172	2639
Nod (iii)	1648	2490
Nod (iv)	773	1708
Colour-magnitude	42	172
Final	170	

TOR in the different filters for all objects, using a Haversine function³. If the separation angle between objects from the spectroscopic and the photometric catalogues is smaller than 0.5 arcsec, we consider the detection to be of the same objects, and hence associate the spectroscopic redshift to the photometric detection. This error is equal to 2.5 MUSE pixels and captures the positional uncertainty on spectroscopic detections.

Out of this step, we attribute a spectroscopic redshift to 20, 25, and 25 sources in the DES, *HST*/WFPC2, and *HST*/ACS catalogues for MACS J0242. In the case of MACS J0949, we attribute a spectroscopic redshift to 54, and 49 sources in the *HST*/ACS and *HST*/WFC3 catalogues.

³The Haversine angle reads as

$$\mathcal{H} = 2 \arcsin \sqrt{\sin^2 \left(\frac{\delta_2 - \delta_1}{2} \right) + \cos \delta_1 \cos \delta_2 \sin^2 \left(\frac{\alpha_2 - \alpha_1}{2} \right)}.$$

3.2.3 Cluster galaxy selection

The next step is the identification of cluster galaxies specifically. For that we are using colour-magnitude selections for each clusters.

The first step consists in applying the red sequence technique (e.g. Gladders & Yee 2000). Using the catalogues after source extraction selections and spectroscopic redshift identification, we compute for both clusters a series of colour-magnitude (CM) diagrams. We compute these for each instrument. As each pass-band represents a magnitude, we can respectively compute 3 and 1 CM diagrams for DES and *HST*/WFPC2 for MACS J0242 (none for *HST*/ACS as only one band is available), and 1 and 6 for *HST*/ACS and *HST*/WFC3 for MACS J0949.

As shown in Fig. 4, cluster members are expected to follow a main sequence (magenta line). To calibrate our selections, we use spectroscopically confirmed cluster members. We then remove all detections with a magnitude exceeding m_{\max} , which varies depending on instruments and filters. For MACS J0242, we have $m_{\max} = 22$ for *HST*/WFPC2, 23.5 for DES/z, and 24.5 for DES/r. For MACS J0949, we have $m_{\max} = 21.5$ for *HST*/WFC3 and 22.5 for *HST*/ACS. We then perform a linear regression and obtain the main sequence. We give in Appendix B the fits for all colour-magnitudes used for both clusters.

Galaxies selected as cluster members are galaxies which have a colour within $2\sigma_C$ of the main red sequence for *HST*/ACS and *HST*/WFC3, and within $3\sigma_C$ for *HST*/WFPC2 and DES. σ_C is the weighed colour standard deviation of the spectroscopically confirmed cluster galaxy sample. These limits are highlighted as black rectangles in Fig. 4. For an instrument with more than two pass-bands, we can compute more than one CM diagram, and thus only retain cluster member identifications compatible with all colour-magnitude diagram selections. We summarize in Tables 4 and 5 for MACS J0242 and MACS J0949, respectively; the number of galaxies identified as cluster members per instrument once these colour-magnitude selections are applied. In some cases, spectroscopically confirmed cluster galaxies fall outside the colour-magnitude selection. These objects are ultimately conserved in our cluster galaxy catalogue. However, we do not include them in the CM cut counts, to show the effect of the photometric selection.

3.2.4 Instrument catalogue combination

We now assemble the galaxy catalogues for each instrument before merging these into a final cluster galaxy catalogue for each cluster. We match the coordinates of sources with the already defined 0.5 arcsec separation angle.

MACS J0242 and MACS J0949 were imaged with different instruments and thus have different coverage. We define the camera of reference as the camera with the highest resolution. In the case of the both clusters, it is *HST*/ACS, but the reference band is chosen as F606W for MACS J0242, and F814W for MACS J0949. MACS J0242 was observed with *HST*/ACS in only one band. Moreover, MACS J0242 was observed with *HST*/WFPC2 in two pass-bands, but the shape of the camera field of view does not cover the entire ACS field of view. MACS J0242 has DES observations in three pass-bands, covering a wide field of view. However the quality of these observations is lower than the ones we have from space. We therefore require for a given cluster member selected galaxy in *HST*/ACS to be at least present in DES or WFPC2 in order to be included into the final cluster member catalogue. MACS J0949 was imaged with *HST*/ACS and WFC3 cameras. *HST*/WFC3 has a smaller field of view than ACS. We detected multiply imaged systems

out of the WFC3 field of view. In order to account for the gravitational effect of individual galaxies on these systems, we include all galaxies detections from at least one camera to our galaxies catalogue.

Finally, cluster galaxies located at a distance larger than 40 arcsec from the cluster centre and with a magnitude difference to the BCG of $\Delta m > 4$ are ignored. Due to their small mass, these galaxies would only have a very small impact on the strong lensing configurations observed.

3.3 Final catalogues

3.3.1 Cluster galaxy catalogues

Section 3.2 describes all the steps for the identification of cluster members, including colour-magnitude selections as well as spectroscopic identifications. All galaxies identified as cluster members and used for our lensing modelling are listed in Appendix, in Tables A3 and A4 for MACS J0242 and MACS J0949. Our final catalogues include 58 and 170 galaxies for MACS J0242 and MACS J0949, respectively.

In order to probe the robustness of our catalogues, we conducted the following verification analysis. We isolated only the spectroscopic detections, and then reinjected them into our photometric selection. We found respectively 15 out of 16 and 34 out of 34 galaxies retained within the photometric selection for MACS J0242 and MACS J0949. As these spectroscopic detections were used to define these selections, they are expected to be selected. Thus, in order to estimate the contamination by galaxies out of the cluster redshift boundaries, we examined the number of selected spectroscopic detections out of the cluster. We find a maximum 2 (2) out of 54 (97) galaxies of our sample contaminants, i.e. 4 per cent (2 per cent) contamination of our sample in cluster MACS J0242 (MACS J0949). Thus, we are confident in our galaxy selection. Nevertheless, for accuracy, we removed these known out-of-cluster galaxies from the final catalogue.

3.3.2 Multiple image systems

In Section 3.1, we described the preliminary steps leading to the multiple image system catalogue. At this point, this is simply a catalogue of reliable detections with redshift $z > 0.6$. The second step in the identification of multiple image systems is to look for similarities between these detections, starting with their spectra. We then look at their positions and see if they are compatible with a lensing geometry. The MUSE field of view being narrower than the *HST* one, one can also look at the colour and morphology of possible multiple images. If a given set of multiple images presents at the same time compatible positions, colours, morphologies and, if available, redshift, we consider them as a multiple image system.

In Fig. 5, we show a colour composite *HST* image of four MUSE detections, four multiple images of the same galaxy located at redshift $z = 4.89$. In the case of MACS J0949, we force extract emission from the MUSE cube corresponding to the location of multiple images previously identified by the RELICS collaboration (obtained through private communication); we only reveal marginal identification as explained in Sec. 5.1.2. The final list of system used in this analysis is presented in Table 8.

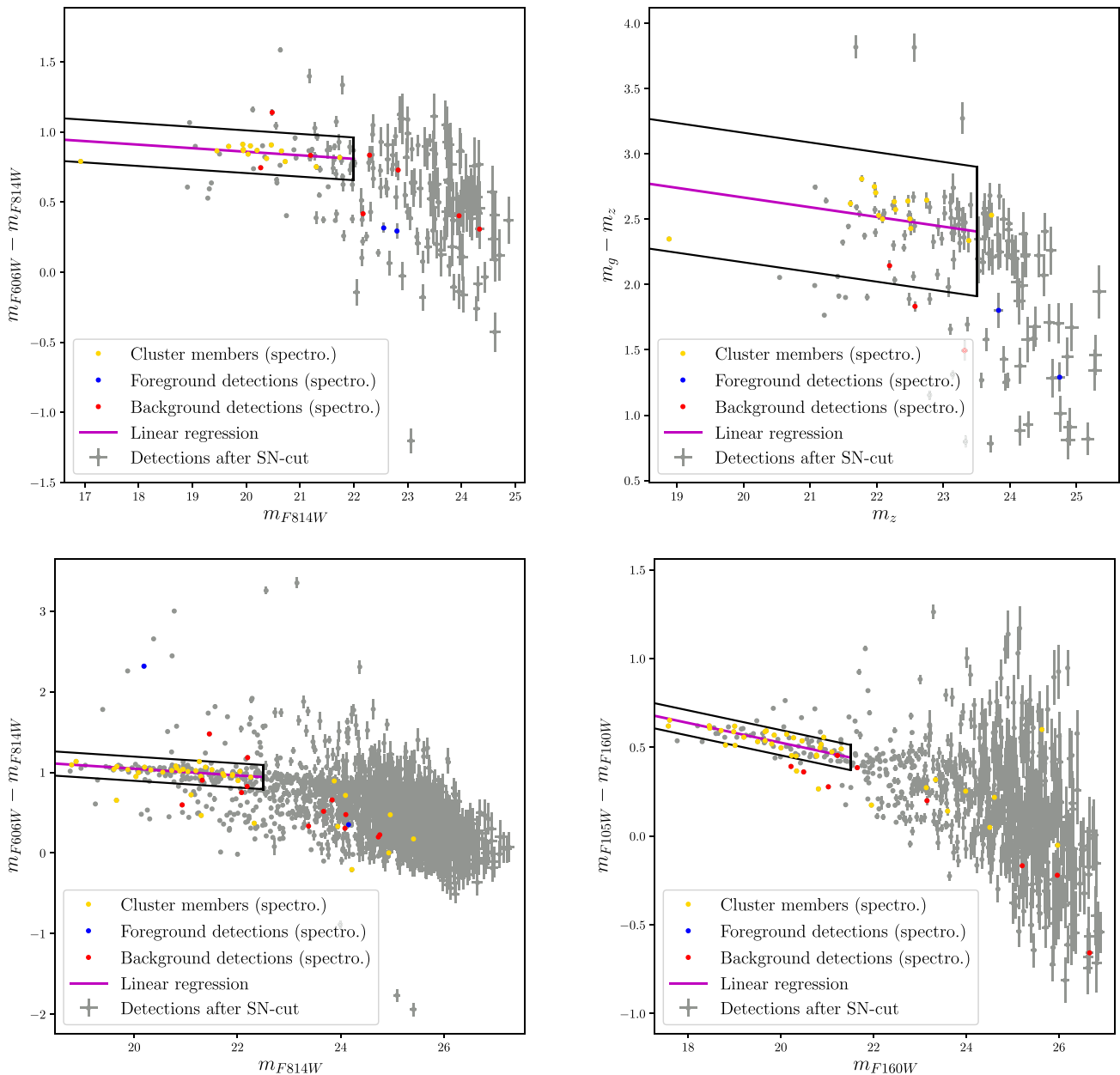


Figure 4. Colour-magnitude diagrams. Top row: cluster MACS J0242. Left panel: instrument *HST*/WFPC2 – m_{F814W} versus $(m_{F606W} - m_{F814W})$. Right panel: Instrument DES – m_z versus $(m_g - m_z)$. Grey filled circles (with their error bars) have successfully passed all selections described in Section 3.2.1. The magenta line represents the main sequence regression. Blue, gold, and red dots represent spectroscopic detections of foreground, cluster, and background objects, respectively. Bottom row: cluster MACS J0949. Left panel: instrument *HST*/ACS – m_{F814W} versus $(m_{F606W} - m_{F814W})$. Right panel: instrument *HST*/WFC3 – m_{F160W} versus $(m_{F105W} - m_{F160W})$.

4 STRONG LENSING MASS MODELLING

The mass distribution of each cluster is reconstructed using the `LENSTOOL` software⁴ (Kneib et al. 1996; Jullo et al. 2007), in its parametric mode. The optimization is performed in the image plane with a Markov Chain Monte-Carlo algorithm (MCMC) assuring the sampling of parameter space. It optimizes the predicted positions of multiple images while fitting an underlying mass distribution composed of large-scale halo(s) to describe the overall cluster

potential, and small-scale halos to account for local perturbers such as cluster galaxies.

For both clusters, we describe any potential using a dual Pseudo-Isothermal Elliptical matter distribution (dPIE, see Kassiola & Kovner 1993) which, as described in Elíasdóttir et al. (2007), has two different pivot scales: a core radius, which describes the potential evolution due to the baryonic matter content, and a *cut radius* that describes the dark matter potential. A dPIE potential is described by seven parameters (excluding the redshift): the central coordinates, the ellipticity e , the position angle θ , the core and cut radii, r_{core} and r_{cut} respectively, and a fiducial central velocity dispersion σ . The

⁴<https://projets.lam.fr/projects/lenstool/wiki>

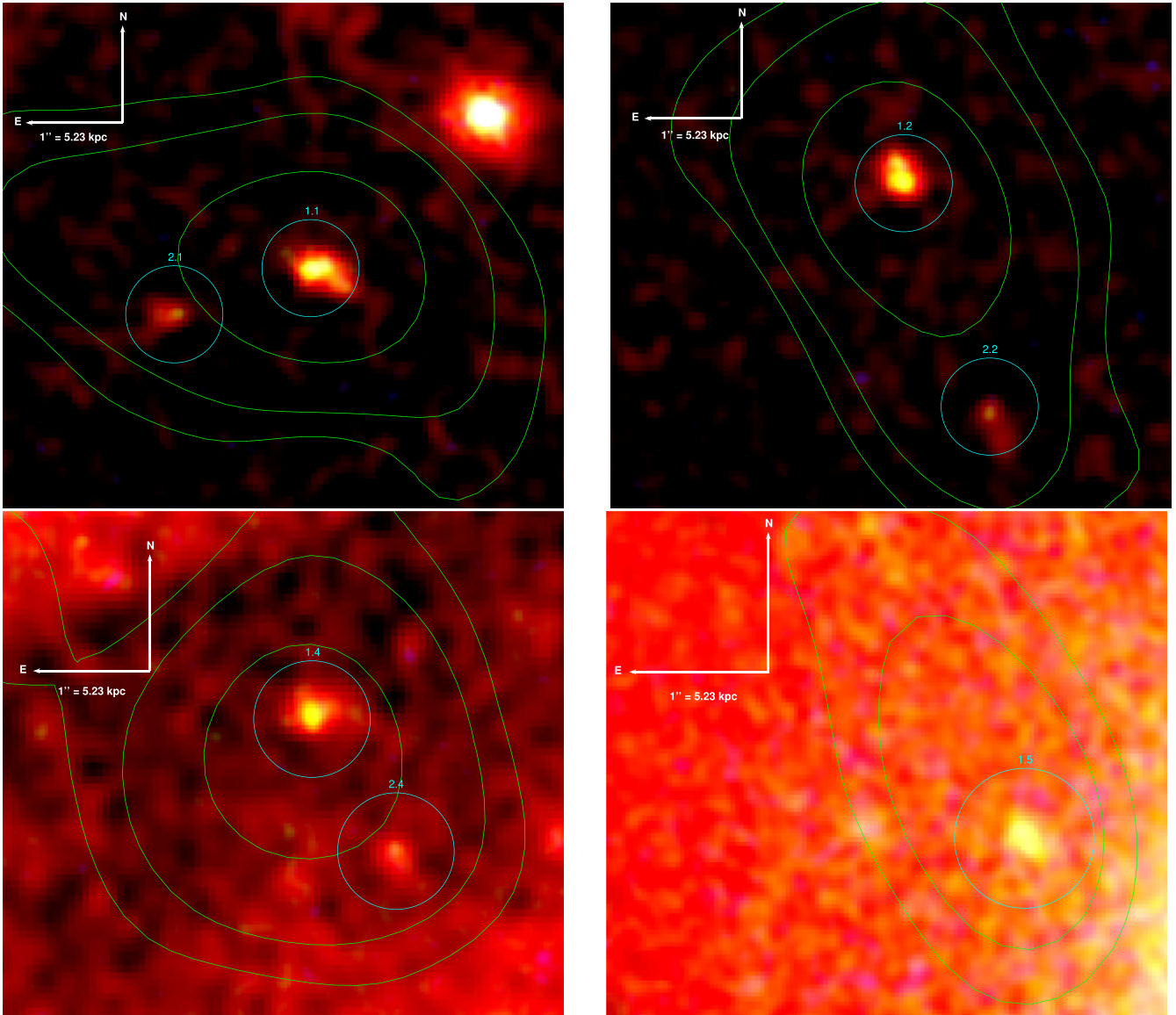


Figure 5. *HST* composite colour image of the four multiple images of System 1 detected in MACS J0949 with VLT/MUSE observations. Colours were enhanced to outline the multiple images. Labelled cyan circles show the positions of the multiple images and correspond to the peak of the Lyman- α emission. The green contours show flux density levels at $1.500, 2.125,$ and $4.000 \times 10^{-20} \text{ erg s}^{-1} \text{ cm}^{-2} \text{ \AA}^{-1}$.

fiducial central velocity dispersion in `LENSTOOL` σ relates to the true three dimensional central velocity dispersion with $\sigma_0 = \sqrt{3/2}\sigma$, as detailed in Bergamini et al. (2019), Appendix C.

For each cluster, we assume one single large-scale dark matter halo to describe the overall cluster potential. It is described by a large velocity dispersion ($\sim 10^3 \text{ km.s}^{-1}$), a large core radius ($\sim 10^2 \text{ kpc}$) and large cut radius. We optimize all the parameters of the potential, excluding the cut radius which we fixed to values $\geq 1 \text{ Mpc}$ as it is located far from the strong lensing region and thus cannot be constrained by multiple images only. The position of each cluster halo is allowed to vary within 10 arcsec of the cluster centre, i.e. the position of the BCG. The ellipticity of the halo is limited to values < 0.8 . The cut radius is fixed to 1.5 Mpc for both MACS J0242 and MACS J0949, as our investigation to model the ICM through lensing shows that this value provides a better fit to the X-ray observations (see our companion paper Allingham et al. in prep.). This value is in agreement with Chang et al. (2018), taking in

consideration the higher mass range of the clusters we are exploring here.

The BCG of each cluster is also modelled independently, using a dPIE potential. The BCG has a strong gravitational influence in the cluster core and will thus impact the geometry of multiple images quite strongly (Newman et al. 2013a). We fix their r_{core} to a small value of 0.30 kpc for cluster MACS J0242 and 0.25 kpc for MACS J0949. For their positions, position angle, and ellipticity, we fix their values to the shape parameters in outputs of `SEXTRACTOR`. Finally, we only optimize its their velocity dispersion and cut radius.

Each individual cluster member is modelled by its own dPIE potential. Their positions, ellipticities, and position angles are obtained with the photometric extraction.

We again assume a small but non-null value for r_{core} . Their cut radii and velocity dispersions are optimized using their magnitude and assuming the Faber–Jackson scaling relation (Faber & Jackson 1976). All cluster members cut radii and velocity dispersions are

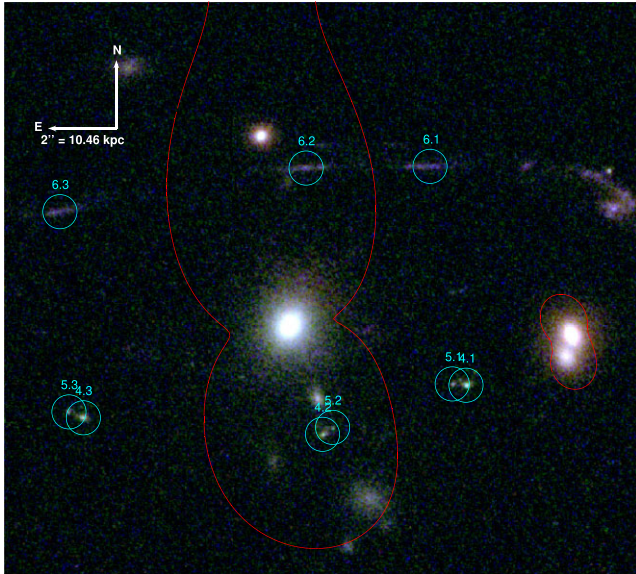


Figure 6. Composite colour *HST* image of the Southern clump in MACS J0949. In cyan, we highlight the positions of the multiple images identified with *HST* and listed in Table 8. The external/tangential critical lines for a source at redshift $z = 3.65$ are represented in red – this redshift being compatible with sources 4, 5, and 6, according to the best fit optimization.

rescaled with regard to a unique set of parameters ($r_{\text{cut},0}$, σ_0). This allows us to optimize each cluster galaxy potential using a remarkably small number of parameters. r_{cut} and σ are allowed to vary between 1 and 50 kpc, and 100 and 300 km.s^{-1} respectively. As mentioned earlier, the Faber–Jackson relation being scaled to a reference magnitude mag_0 , we use the reference pass-band of the main camera for each cluster, ACS/F606W ($mag_0 = 20.0205$) and ACS/F814W ($mag_0 = 19.5085$) for MACS J0242 and MACS J0949, respectively.

As the centre of the cluster-scale halo and the BCG are aligned, the r_{core} , r_{cut} , and σ parameters of both potentials are degenerate. Due to the limited number of lensing constraints, we proceed incrementally to model the potential, to narrow the parameters space. First, we include the BCG in the scaling relation of the cluster galaxies and optimize the cluster-scale halo and the scaling relation parameters as described above. Second, we run a model with the BCG optimized independently, only optimizing r_{cut} and σ as explained above. However in this case, the cluster-scale halo parameters are allowed to vary within a restricted range, defined Gaussianly around the best fit values obtained from the first model. This way, we can limit the degeneracy between the cluster-scale and BCG halos, and obtain physical values to describe the BCG potential.

Finally, we added a completely free dPIE potential south to the main cluster halo of MACS J0949. This structure has already been included in the public RELICS models and correspond to the location of three candidate multiply-imaged systems 4, 5, and 6 as shown in Fig. 6. We optimized their redshifts as well as the potential and to prevent nonphysically high value we imposed Gaussian priors on r_{core} , r_{cut} , and velocity dispersion.

Table 6. List of multiple images detected with VLT/MUSE in MACS J0242. We here list their ID, coordinates, R.A. and Decl., given in degrees (J2000), and their measured spectroscopic redshift z .

Id.	R.A.	Decl.	z
1.1	40.6574070	−21.5383801	3.0627
1.2	40.6575168	−21.5387136	3.0627
1.3	40.6531265	−21.5473860	3.0627
1.4	40.6446350	−21.5392391	3.0627
2.1	40.6453464	−21.5336906	3.8681
2.2	40.6411296	−21.5407791	3.8681
2.3	40.6419142	−21.5436276	3.8681
2.4	40.6546554	−21.5416287	3.8681
3.1	40.6580815	−21.5363952	3.8682
3.2	40.6454775	−21.5404581	3.8682
4.1	40.6523889	−21.5446358	3.0615
4.2	40.6499994	−21.5316520	3.0615
5.1	40.6529585	−21.5386743	4.9492
5.2	40.6432539	−21.5482627	4.9492
6.1	40.6499320	−21.5354918	1.3010
6.2	40.6541677	−21.5382729	1.3010
6.3	40.6463323	−21.5366811	1.3010
6.4	40.6479134	−21.5470977	1.3010

5 RESULTS

5.1 Strong lensing mass models

5.1.1 MACS J0242 model

In MACS J0242, we detected six systems of multiple images with MUSE. Their positions and redshifts are given in Table 6. We provide the best fit parameters of our model in Table 7. The fixed values are highlighted by an asterisk. Our best-fit model yields predicted multiple images with a rms of 0.39 arcsec of the observed positions. The inclusion of an external shear component does not provide a significant improvement to the mass model, i.e. a rms of 0.38 arcsec compared to our best-fit mass model of 0.39 arcsec. This error is smaller than the positional error associated to spectroscopic detections. However, the error on the position of the multiply-lensed images is associated to their photometric detections, with much smaller positional error.

The geometry of the cluster is typical of a relaxed cool-core cluster. The density profiles peak in the centre, and the transition between the BCG and the DM halo appears to be very smooth as illustrated in Fig. 7. No other significant structure are identified. Fig. 7 shows the surface density profile, Σ , and includes a 68 per cent confidence interval around the best contours, as a function of the distance to the cluster centre. The inner part of the profile, $R \leq 50$ kpc, is dominated by the BCG potential, whereas at larger radii, the dark matter halo takes over. This pivot scale of about 50 kpc corresponds to the core radius of the DM halo, and the separation between the two different regimes of the dPIE potential. However, disentangling the potential influence of the BCG and the DM of the halo would require a much finer study of the stellar mass distribution of the BCG with a spectral energy distribution (SED) fit, which is beyond the scope of this article.

We find the total density profile (baryonic and dark matter) of MACS J0242 to be well fitted by a Navarro–Frenk–White profile (NFW, see Navarro, Frenk & White 1996) in the region between 20 and 1000 kpc. We limit the reconstruction to radii $r \geq 20$ kpc as the Kron-like magnitude radius of the BCG is about 10 kpc, and we attempt to limit the influence of stellar physics within the fit.

Table 7. Best fit parameters of the strong lensing mass models for MACS J0242 and MACS J0949. We here list the central coordinates, Δ_α and Δ_δ in arcsec, relative to the centre, the ellipticity, e , the position angle in degrees, θ , the core radius in kpc, r_{core} , the cut radius in kpc, r_{cut} , and the velocity dispersion in km.s^{-1} , σ , for each component of the model. The centres are taken to be respectively $(\alpha_c, \delta_c) = (40.649555, -21.540485)$ deg and $(\alpha_c, \delta_c) = (147.4659012, 17.1195939)$ deg for MACS J0242 and MACS J0949. The asterisks highlight parameters which are fixed during the optimization.

	Δ_α	Δ_δ	e	θ	r_{core}	r_{cut}	σ
MACS J0242							
DM halo	$-0.138^{+0.085}_{-0.143}$	$0.136^{+0.111}_{-0.179}$	$0.287^{+0.037}_{-0.027}$	$17.884^{+0.762}_{-1.830}$	$57.194^{+6.044}_{-8.414}$	1500*	$918.479^{+28.984}_{-36.074}$
BCG	0.044*	-0.090*	0.226*	$155.758^{+10.766}_{-9.604}$	0.300*	$177.575^{+32.245}_{-57.950}$	$524.516^{+58.810}_{-43.956}$
Galaxy catalogue					0.030*	$5.625^{+7.845}_{-1.808}$	$199.242^{+30.721}_{-53.257}$
MACS J0949							
DM halo	$-1.936^{+0.215}_{-2.843}$	$-0.671^{+0.565}_{-0.666}$	$0.249^{+0.398}_{-0.045}$	$92.434^{+0.570}_{-1.289}$	$116.246^{+24.108}_{-51.661}$	1500*	$1236.094^{+59.307}_{-310.553}$
Southern halo	$4.800^{+0.748}_{-0.464}$	$-60.133^{+2.391}_{-1.417}$	$0.097^{+0.294}_{-0.061}$	$128.629^{+41.438}_{-27.521}$	$20.548^{+31.596}_{-8.771}$	$232.502^{+180.124}_{-119.902}$	$323.220^{+120.202}_{-54.851}$
BCG	0*	0*	0.475*	120.130*	0.250*	$98.044^{+153.739}_{-34.342}$	$253.749^{+196.474}_{-18.473}$
Galaxy catalogue					0.150*	$23.135^{+111.473}_{-2.053}$	$139.314^{+25.804}_{-18.547}$

Table 8. List of the multiple images detected with VLT/MUSE in MACS J0949. We here list their ID, coordinates, R.A. and Decl. given in degrees (J2000), and their measured spectroscopic redshift z . Values within brackets were obtained after L_{EN}STOOL redshift optimization.

Id.	R.A.	Decl.	z
1.1	147.4683753	17.11409360	4.8902
1.2	147.4738000	17.11754490	4.8902
1.3	147.4561230	17.11911410	4.8902
1.4	147.4687438	17.12369520	4.8902
1.5	147.4668972	17.12016960	4.8902
2.1	147.4687829	17.11396160	4.8844
2.2	147.4735428	17.11690610	4.8844
2.3	147.4560463	17.11877380	4.8844
2.4	147.4685346	17.12338060	4.8844
3.1	147.4702800	17.11513600	$[4.85^{+1.52}_{-0.70}]$
3.2	147.4714400	17.11579400	$[4.85^{+1.52}_{-0.70}]$
4.1	147.4630587	17.10291430	$[3.76^{+1.57}_{-0.80}]$
4.2	147.4642781	17.10251570	$[3.76^{+1.57}_{-0.80}]$
4.3	147.4663104	17.10264970	$[3.76^{+1.57}_{-0.80}]$
5.1	147.4631754	17.10292500	$[3.63^{+1.67}_{-0.74}]$
5.2	147.4641921	17.10257190	$[3.63^{+1.67}_{-0.74}]$
5.3	147.4664329	17.10269780	$[3.63^{+1.67}_{-0.74}]$
6.1	147.4633639	17.10469208	$[3.57^{+0.35}_{-1.08}]$
6.2	147.4644174	17.10467818	$[3.57^{+0.35}_{-1.08}]$
6.3	147.4665100	17.10432399	$[3.57^{+0.35}_{-1.08}]$

In order to compare it to the NFW fit of cluster MACS J0949, we arbitrarily take 20 kpc to be a good compromise of strong lensing potential reconstruction without stellar physics contamination. For regions $r > 200$ kpc, the cluster-scale DM halo should dominate the whole matter distribution. As the DM halo dPIE parameters ρ_0 and r_{core} are well constrained through strong lensing, this region beyond multiple images constraints and below the cut-off radius r_{cut} is expected to be well represented by a NFW profile. With NFW parameters $\rho_s = 3.42 \times 10^{-22} \text{ kg m}^{-3}$ and $r_s = 209.9$ kpc, we find a reduced $\chi^2 = 1.11$.

In order to compare our results to the X-ray data, we extrapolate the masses $M_{\Delta, c}$ comprised within an overdensity Δ using

$$R_\Delta = \left\{ R \left| \frac{M(< R)}{\frac{4}{3}\pi R^3} = \Delta \cdot \rho_c(z) \right. \right\}, \quad (1)$$

where ρ_c is the critical density at the cluster redshift, and $M(< R)$ the total mass enclosed within a given radius, R . At large radii ($R > 200$ kpc), the strong lensing mass reconstruction only provides an estimate of the true mass distribution as there is no strong lensing constraints to precisely and accurately estimate the mass distribution in the outskirts. It therefore only provides a pure extrapolation of the inner core mass distribution, and only a weak-lensing analysis would provide a precise mass estimate in this region of the cluster; however, this is beyond the scope of this analysis. We also compute $M_{2D}(R < 200 \text{ kpc})$, the integrated mass within a radius of 200 kpc. This mass is a direct output of the lensing mass reconstruction. These values are all listed in Table 9.

5.1.2 MACS J0949 model

In MACS J0949, we identified several objects located behind the cluster with the MUSE observations. However, most of them appear to be singly lensed. Through the techniques exposed in Section 3, we detected a multiple image system in the MUSE field at redshift $z = 4.8902$. This system 1 is composed of five multiple images, including four in the field, and one counterpart 1.3 located outside the MUSE field of view, and detected in the *HST* imaging. We also detect a fifth image, image 1.5, located close the BCG of the cluster. Images 1.4 and 1.5 (see Fig. 2), straddling the central critical curve of the cluster, allow to set stringent constraints on the inner slope of the mass density profile (as exhibited in Schneider, Ehlers & Falco 1992; Newman et al. 2013b; Caminha et al. 2017).

Careful consideration of the *HST* images allowed us to detect secondary, fainter emission knots for four multiple images in system 1 – all except the central one which is hidden by the emission of the BCG. This is shown in Fig. 5. The MUSE spectroscopic analysis of these three images which compose system 2 shows a faint Ly- α peak for all of them, allowing us to measure a redshift of 4.8844, very close to that of system 1. We interpret system 2 either as part of the same galaxy, or a companion galaxy of system 1’s source. The Ly- α halo of system 1 extends, and the potential secondary peak emission coincides with system 2 emission knots. We include 4 multiple images of system 2 as additional constraints to our mass model, the fifth image being demagnified we restrain ourselves from including it in our mass model. The coordinates and redshifts of the multiply imaged systems are given in Table 8. We give a list of the singly imaged objects in Appendix A.

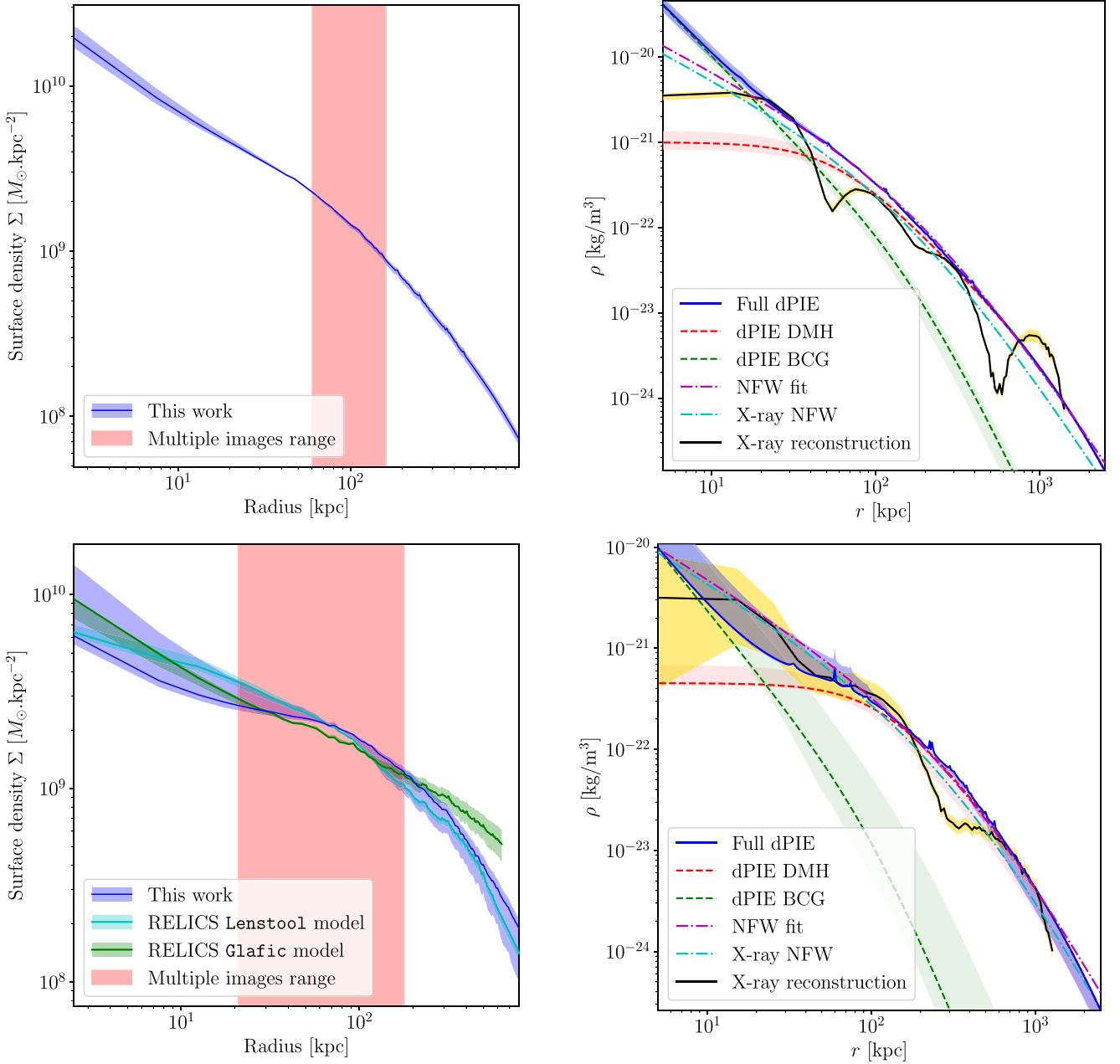


Figure 7. Top row: cluster MACS J0242. Left panel: surface mass density profile derived from the best-fit mass model. Shaded regions show the 68 per cent confidence interval. We display in red the range of the multiple images, and thus the regions in which the constraints are the most stringent. – Right panel: volume mass density. The reconstruction of the *XMM–Newton* observations are shown in black, given with 1σ error bars in yellow. The green and red curves – with error bars – represent respectively the BCG and DM halo reconstructions, and the full cluster is shown in blue. The magenta dashed line represents the NFW fit of the total density from LENSTOOL reconstruction – all galaxies and DM halo. The cyan line shows the fit to the X-ray data. Bottom row: cluster MACS J0949. Blue: our model, with 68 per cent confidence interval. Cyan: LENSTOOL model from RELICS. We note that error bars were obtained on a different sample (2000 realizations for our model, 100 for RELICS). Green: GLAFIC RELICS model, realized under the same conditions. Red: region of the multiple images constraints – Right panel: volume mass density. The reconstruction of the *XMM–Newton* data is shown in black, given with 1σ error bars in yellow. The green and red curves represent respectively the BCG and DM halo reconstruction, and the full cluster is shown in blue. The magenta dashed line represents the NFW fit to the LENSTOOL reconstruction. The cyan line shows the fit to the X-ray data.

The inspection of *HST* images also led to the discovery of system 3, composed of two multiple images. These faint detections in the South of the cluster were equally present in the MUSE field. A faint and a priori inconclusive detection of Ly- α – see Fig. 8 – is consistent with the redshift optimization of this system using only system 1, or 1 and 2 as constraints. We therefore conclude that this system’s redshift is

5.8658. However the stack of the spectra presents a S/N ratio < 2 , and the MUSE data are sensible to sky perturbations in the speculated Ly- α bandwidth. We therefore decide not to use this as a redshift constraint, but to let the redshift free during the model optimization.

At last, we detect three candidate multiply lensed images in the South of the *HST* field of view, in a region not covered by the MUSE

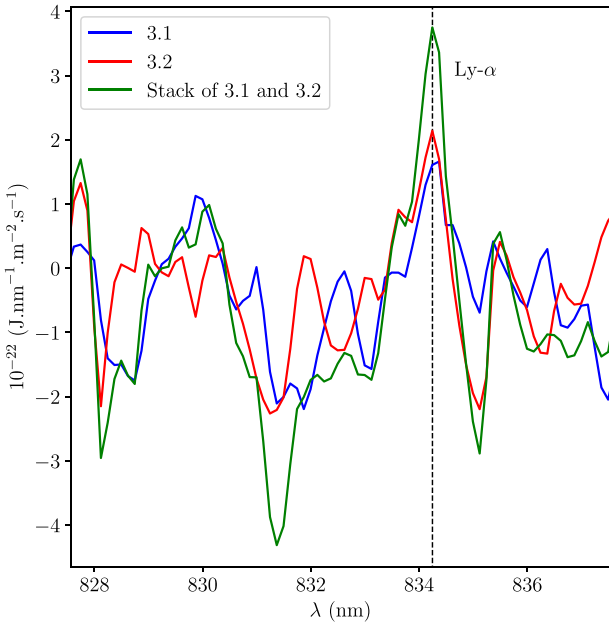


Figure 8. Spectra of images 3.1 and 3.2 of cluster MACS J0949 obtained by VLT/MUSE. We can observe a faint signal, possibly Ly- α . Blue: spectrum of 3.1; Red: spectrum of 3.2; Green: summed spectra. The redshift measured would be of 5.8658. However, the confidence level of our measurements is low due to high sky noise at this wavelength.

observations. We included these three candidate systems 4, 5, and 6 in our mass model, letting their redshifts as free parameters. Their detection supposes the presence of a Southern halo as described in Section 4. For systems 3, 4, 5, and 6, our best fit mass model gives the respective redshifts: $4.85^{+1.52}_{-0.70}$, $3.76^{+1.57}_{-0.80}$, $3.63^{+1.67}_{-0.74}$ and $3.57^{+0.35}_{-1.08}$.

Similarly to MACS J0242, we model the mass distribution of the cluster scale halo and the BCG galaxy separately. The best-fit mass model parameters are listed in Table 7, and gives a rms of 0.15 arcsec. The addition of an external shear component does not improve the mass model, and gives a rms of 0.16 arcsec. In a similar fashion to MACS J0242, although the degeneracy between the cluster scale halo and the BCG is still present, the BCG optimization converges. The rms is particularly small which may be explained by the lack of constraints in our model. Indeed, as shown in e.g. Johnson & Sharon (2016), a larger number of constraints may increase the value of the rms but could also improve the accuracy of the model. Similarly to MACS J0242, we compute integrated and 3D masses for MACS J0949. These are listed in Table 9 and discussed further in Section 6.

We compare our model of MACS J0949 to the two publicly available models from the RELICS collaboration⁵ Comparing the surface density profiles, we find a 1σ agreement between the model presented in this article and the LENSTOOL RELICS model as can be seen in Fig. 7. As for the RELICS model obtained using the GLAFIC lensing algorithm (presented in Oguri 2010), its density profile is in agreement with our model, although the most stringent constraints (in the $R \in [40, 100]$ kpc region) yield a slightly smaller surface density. The overall profile from the LENSTOOL RELICS public release model presents a flatter density profile and an excess in mass after 80 kpc (coincidental with the Einstein radius of system

1). This could be partially explained by the more massive structure in the South of the cluster, which is slightly offset from the South bright galaxy surrounded by systems 4, 5, and 6 as mentioned before ($M_{2D}(< 100 \text{ kpc}) = 13.02 \times 10^{12} M_{\odot}$ compared to $M_{2D}(< 100 \text{ kpc}) = 7.65 \times 10^{12} M_{\odot}$ for our model). We report a very good agreement between the measured spectroscopic redshift obtained from MUSE observations with the photo- z used by the RELICS team (obtained through private communication with K. Sharon). Our model presents a significantly lower rms of 0.15 arcsec, in comparison to 0.58 arcsec.

The reconstructed mass distribution appears to be more elliptical than the X-ray surface brightness obtained with *XMM-Newton* as shown in Fig. 2. The three-dimensional (3D) density profile is presented in Fig. 7. It confirms the inflexion point in the density profile at $r \simeq 100$ kpc, and therefore suggests that the cluster is still undergoing a relaxing phase. The NFW profile fit in the $r \in [20, 1000]$ kpc region yields NFW parameters $\rho_S = 1.23 \times 10^{-22} \text{ kg m}^{-3}$, $r_S = 405.5$ kpc, for a reduced $\chi^2 = 1.90$. The quality of this fit is thus not comparable to that of cluster MACS J0242, mostly due to the flatter density profile in the $R \in [40, 100]$ kpc region.

Looking at the galaxy distribution within the cluster, we observe four bright and massive galaxies, of comparable magnitude to the BCG.⁶ We could extrapolate all of these bright galaxies to have been the BCG of former galaxy clusters, which would have merged with MACS J0949 in the past. However, the X-ray observations show a diffuse emission centred on the BCG and thus do not provide any evidence of recent merger events. Therefore, our analysis strongly suggests a unique dominant cluster scale dark matter component. Nonetheless, we stress that the magnitude gap between the BCG and the second-brightest cluster galaxy in MACS J0242 is much larger than in MACS J0949. According to Trevisan & Mamon (2017), this is an additional argument to claim that the former cluster is more relaxed, and that MACS J0949 went through a recent merging event.

Our interpretation of the dynamical state of MACS J0949 and its lensing power could be further constrained with additional spectroscopic or imaging observations. The clear identification of the spectroscopic redshift of system 3, and of additional systems would particularly assist constraining the dark matter halo ellipticity, core radius, and velocity dispersion.

5.1.3 Relensing in MACS J0949

On Fig. 9, we display the extracted emission of images 1.1 and 2.1 detected in MACS J0949 from the MUSE narrow-band centred on $\lambda = 715.869$ nm within a yellow box. In order to verify the robustness of the lensing model of MACS J0949, we then infer the emission in the source plane ($z = 4.8902$), before projecting it back to the image plane with our lens model, to obtain a relensed prediction.

The other multiple images on the MUSE field, 1.2, 1.4, 1.5, 2.2, and 2.4 are correctly predicted. Their Lyman- α detections are also listed in Table 8. Images 1.4 and 1.5 emission appear to be connected. This is simply due to the extended source emission of systems 1 and 2, as a number of faint multiple images of system 2 are predicted between 1.4 and 1.5, in agreement to the MUSE observations on the narrow-band.

⁵<https://archive.stsci.edu/prepds/relics/>

⁶The maximum magnitude separation between these five galaxies being 0.29 on the reference band ACS/F814W.

Table 9. Mass and radius measurements for MACS J0242 and MACS J0949. All error bars show a 68 % confidence interval. We here list M_* , the stellar mass, $M_{2D}(R < 200\text{ kpc})$, the mass distribution obtained in projection on the plane of the cluster, within a radius of 200 kpc, and M_Δ and R_Δ , defined in equation (1). Masses are given in $10^{14} M_\odot$ and distances in kpc. The X-ray masses are following the NFW fit.

Mass ($10^{14} M_\odot$)	MACS J0242		MACS J0949	
	Lensing	X-ray	Lensing	X-ray
M_*	0.065 ± 0.006		0.139 ± 0.014	
$M_{2D}(R < 200\text{ kpc})$	$1.667^{+0.032}_{-0.052}$	$1.163^{+0.036}_{-0.039}$	$1.996^{+0.051}_{-0.199}$	$1.635^{+0.065}_{-0.072}$
M_{2500}	$3.113^{+0.160}_{-0.200}$	$1.875^{+0.070}_{-0.069}$	$5.621^{+0.122}_{-0.942}$	$3.439^{+0.281}_{-0.266}$
M_{1000}	$4.628^{+0.289}_{-0.342}$	$2.695^{+0.122}_{-0.121}$	$8.848^{+0.000}_{-2.215}$	$5.547^{+0.778}_{-0.693}$
M_{500}	$5.954^{+0.400}_{-0.455}$	$3.379^{+0.168}_{-0.168}$	$11.483^{+0.000}_{-3.417}$	$7.429^{+1.310}_{-1.137}$
M_{200}	$7.748^{+0.538}_{-0.598}$	$4.343^{+0.238}_{-0.237}$	$14.790^{+0.000}_{-4.824}$	$10.165^{+2.234}_{-1.799}$

Radius (kpc)	MACS J0242		MACS J0949	
	Lensing	X-ray	Lensing	X-ray
R_{2500}	$541.2^{+9.1}_{-11.9}$	466^{+5}_{-6}	$641.7^{+4.6}_{-38.1}$	555^{+15}_{-15}
R_{1000}	$838.3^{+17.1}_{-21.2}$	713^{+11}_{-11}	$1013.2^{+0.0}_{-92.8}$	884^{+39}_{-39}
R_{500}	$1148.7^{+25.2}_{-30.1}$	969^{+16}_{-16}	$1392.4^{+0.0}_{-154.6}$	1227^{+68}_{-66}
R_{200}	$1702.0^{+38.5}_{-45.0}$	1430^{+26}_{-27}	$2056.1^{+0.0}_{-253.5}$	1849^{+126}_{-116}

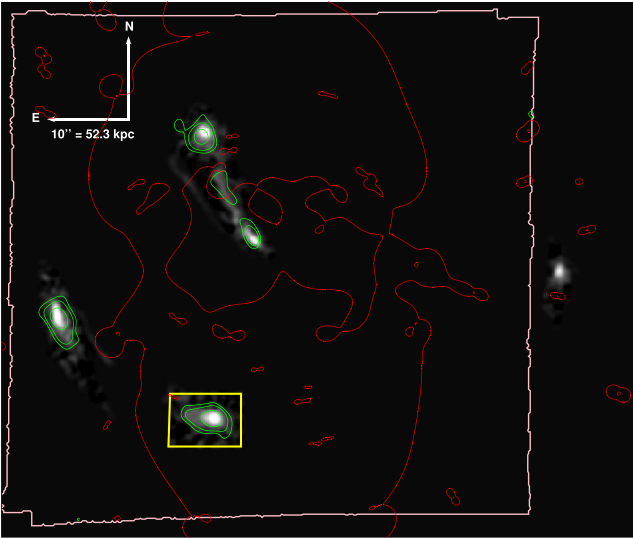


Figure 9. MACS J0949 reconstruction of the full image plane of system 1 from the unique extended emission images 1.1 and 2.1. Their region, highlighted with the yellow box is cut out and deprojected into the source plane, and casted back in the image plane to produce the full system. We clearly observe a continuous emission between the North-East image 1.4 and the central one 1.5. We display in green the contours of the Ly- α extended emission from the VLT/MUSE narrow-band image centred at 715.869 nm and 1.625 nm wide, showing the four detected multiple images of system 1, and three of system 2 (see Fig. 2 for more details). The last images 1.3 and 2.3 of these systems are located outside of the VLT/MUSE field of view. The critical lines are displayed in red, for redshift $z = 4.8902$ of system 1. The pink overlay represents the MUSE narrow-band contours.

5.2 Stellar mass estimate

The strong lensing analyses are giving us an estimate of the total mass enclosed in each clusters.

We further compare our strong lensing mass with an estimate stellar mass. We use the reference cluster members catalogue magnitudes

described in Section 3, converted into K-band luminosity L_K ,⁷ and use it as a proxy for stellar mass. For the scaling relations we refer the reader to Hogg et al. (2002); Lin et al. (2006). These catalogues were established over the entire observable clusters, although the faintest galaxies were cut out beyond distances of 40 arcsec from the centre.

Once the L_K catalogue established, we adapt the Salpeter initial mass function, and use the mass-to-light relationship for red quiescent galaxies derived by Arnouts et al. (2007) on the SWIRE-VVDS-CFHTLS surveys, based on the Bruzual & Charlot (2003) stellar population models:

$$\log_{10} \left[\frac{M_*}{M_\odot} \frac{L_\odot}{L_K} \right] = az + b, \quad (2)$$

given the parameters $\{a, b\} = \{-0.18 \pm 0.04, +0.07 \pm 0.04\}$. While we acknowledge our studied clusters are within a redshift range presenting large uncertainties in the relationship presented in Arnouts et al. (2007, see Fig. 9), we refer the reader to the detailed comparison made in Appendix D, Fig. 28 of Ilbert et al. (2010). Although the former appears to overestimate the stellar mass by an average 0.2 dex for red sequence galaxies, it also appears to be reasonably well calibrated for $z \in [0.3, 0.4]$. We present the inferred stellar masses for both clusters in Table 9.

In order to have a theoretical reference, we compare our estimates with the stellar mass predicted using the formula derived by Giodini et al. (2009). This relationship, established for poor clusters, with redshifts $0.1 \leq z \leq 1$, relates the total mass of the cluster to its stellar fraction (M_*/M_{500} here) using the relation:

$$f_{500}^* = 0.05^{+0.001}_{-0.001} \left(\frac{M_{500}}{5 \times 10^{13} M_\odot} \right)^{-0.37 \pm 0.04}. \quad (3)$$

Let us notice the high (~ 50 per cent) logarithmic scatter in the data fitting this relationship. As this relationship was established using X-ray measurements of M_{500} , and that strong lensing is not a direct probe of this value, we use the NFW reconstruction obtained through X-ray for the M_{500} values (see Fig. 7).

⁷We take the K-band reference here to be the KPNO Flamingos Ks filter.

Table 10. Comparison between the star fractions $f_{500}^* = M_*/M_{500}$ measured with this work and the predictions from the Giodini et al. (2009) formula. M_{500} is taken to be the NFW X-ray extrapolated value. All results are in percentage.

$f_{500}^*(\%)$	MACS J0242	MACS J0949
This work	1.919 ± 0.205	1.873 ± 0.360
Prediction	2.466 ± 0.334	1.842 ± 0.407

For MACS J0242, the field of view considered is quite large (DES: 182 arcsec), as we consider all galaxy in *HST*/WFPC2 or DES, and thus our cluster member catalogue is assumed to be relatively complete. We measure a stellar mass $M_* = (6.484 \pm 0.615) \times 10^{12} M_\odot$ for MACS J0242. Let us notice these error bars are only associated to the error on the measured magnitude and the parameters a and b equation (2). We obtain a difference between our measured value and the predicted value of $M_{*,\text{Giodini}} = (8.332 \pm 1.128) \times 10^{12} M_\odot$. We may explain this discrepancy by the variable conditions for selecting a galaxy within the galaxy catalogue. Indeed, the field of view being different between WFPC2, ACS, and DES, as well as the poorer imaging quality of the latter instrument, we expect our error bars to be far larger than those computed given the error on the measured magnitude.

For MACS J0949, we require that a galaxy is detected in either *HST*/ACS or *HST*/WFC3 to include it in the final catalogue. Because the field of view of WFC3 is smaller than that of ACS, a large number of selected cluster member galaxies are weakly constrained, as ACS only contains two bands here. This method is adapted to our lensing analysis, the main goal of this paper, as galaxies far from the cluster centre are particularly important to constrain the southern halo. However, when considering the stellar content of the cluster, we might be selecting too many galaxies. Our analysis yields $M_* = (1.392 \pm 0.137) \times 10^{13} M_\odot$. Similarly to MACS J0242, we compare our measurement with the predicted value following the Giodini et al. (2009) formula. We obtain a stellar mass $M_{*,\text{Giodini}} = (1.369 \pm 0.302) \times 10^{13} M_\odot$. This difference, however small, can give us an estimate of the overestimation of our cluster member catalogue. We summarize the estimated stellar fractions for both clusters, $f_{500}^* = M_*/M_{500}$, as well as the predicted values with the Giodini et al. (2009) formula in Table 10.

5.3 X-ray analysis

5.3.1 Analysis procedure

We used the X-COP analysis pipeline (Ghirardini et al. 2019) to analyse the data and compute the hydrostatic mass profiles of the two systems. We extracted X-ray photon images in the [0.7–1.2] keV band, which maximizes the signal-to-background ratio. To estimate the non-X-ray background, we used the unexposed corners of the MOS detectors to estimate the cosmic-ray-induced flux at the time of the observations. The difference between the scaled high-energy count rates inside and outside the field of view were then used to estimate the residual soft proton contribution, which was next modelled following the method described in Ghirardini et al. (2018). To determine the spectroscopic temperature profile of the two systems, we extracted spectra in logarithmically spaced concentric annuli centred on the surface brightness peak. The sky background emission was measured in regions located well outside of the cluster’s virial radius and described by a three-component model including the cosmic X-ray background, the local hot bubble, and the galactic

halo. The sky background spectrum was then rescaled appropriately to the source regions and added as an additional model component. Finally, the source spectrum was modelled by a single-temperature APEC model (Smith et al. 2001) absorbed by the Galactic N_H , which was fixed to the HI4PI value (HI4PI Collaboration et al. 2016).

5.3.2 Hydrostatic mass reconstruction

We used the publicly available Python package `hydromass`⁸ (Eckert et al. 2022) to deproject the X-ray data and recover the mass under the hypothesis of hydrostatic equilibrium. The X-ray surface brightness and spectroscopic temperature profiles are fitted jointly using a NFW profile to recover the X-ray mass profile. The technique employed here is similar to the method described in Ettori et al. (2019), in which the gas density profile and the parametric mass profile are used to integrate the hydrostatic equilibrium equation and predict the 3D pressure and temperature profiles. The 3D temperature profile is then projected along the line of sight using spectroscopic-like weights (Mazzotta et al. 2004) and adjusted onto the observed spectroscopic temperature profile. The model temperature and gas density profiles are convolved with the *XMM-Newton* PSF to correct for the smearing introduced by the telescope’s spatial resolution, in particular in the cluster’s central regions.

5.3.3 MACS J0242

MACS J0242 exhibits all the features of a relaxed, cool-core cluster. Its X-ray morphology is regular and it shows a pronounced surface brightness peak, a central temperature drop, and a metal abundance peak in its core. The dynamical state of the cluster is best gauged from the X-ray emission, but the optical emission lines of the BCG is an additional, relatively faithful tracer of the presence of a cool core. The NFW mass reconstruction returns a mass $M_{500} = (3.4 \pm 0.2) \times 10^{14} M_\odot$. In order to compare it directly to the lensing mass where multiply imaged systems yield important constraints, we project the NFW density in two-dimensional (2D) and compute $M_{2D}(< 200 \text{ kpc}) = 1.163^{+0.036}_{-0.039} \times 10^{14} M_\odot$. For an average temperature of 4.5 keV, this is in agreement with the expectations of mass-temperature relations (e.g. Lovisari et al. 2020). The cluster appears to be highly concentrated, with a fitted NFW concentration $c_{200} = 8.2 \pm 0.5$. At 200 kpc, X-ray observations suggest the gas fraction to be $f_{g,200 \text{ kpc}} = 0.115^{+0.003}_{-0.004}$. The ellipticity of the cluster obtained with our lensing mass model is not recovered by the X-ray analysis, as it presents a spherical surface brightness. The ICM has its own dynamics and thus is not expected to present a similar ellipticity to the total density of matter. The discrepancy between the ICM and DM halo ellipticity is documented in e.g. (Lee & Suto 2003; Debattista et al. 2008; Lau et al. 2012; Umetsu et al. 2018; Stapelberg et al. 2022). It stems from the collisional character of baryons, allowing the ICM to geometrically relax faster than the cold dark matter halo counterpart, non-collisional.

5.3.4 MACS J0949

MACS J0949 exhibits a regular X-ray morphology with no obvious large substructure. However, its brightness distribution is relatively flat, it shows a high central entropy and central cooling time, and no temperature drop in its core. Therefore, MACS J0949 is not a

⁸<https://github.com/domeckert/hydromass>

relaxed cool-core cluster, but its regular morphology indicates that it is not strongly disturbed either. Such properties are typical of post-merger clusters in the process of relaxation after a merging event. The hydrostatic mass profile is well described by an NFW model with $c_{200} = 5.3^{+1.3}_{-1.0}$ and $M_{500} = 7.4^{+1.4}_{-1.2} \times 10^{14} M_{\odot}$. The NFW projected mass yields $M_{2D}(< 200\text{kpc}) = 1.635^{+0.065}_{-0.072} \times 10^{14} M_{\odot}$. Its hydrostatic gas fraction $f_{g,500} = 0.155^{+0.016}_{-0.014}$ is consistent with the Universal baryon fraction (Ade et al. 2016). At 200 kpc, the same gas fraction is measured at $f_{g,200\text{kpc}} = 0.053^{+0.007}_{-0.006}$. Similarly to MACS J0242, the X-ray signal does not present any ellipticity.

6 DISCUSSION AND CONCLUSION

In order to reconstruct the mass distribution of strong lensing galaxy clusters MACS J0242 and MACS J0949, we have used the combination of imaging (*HST*, *DES*) and spectroscopic (*VLT/MUSE*) surveys to detect, respectively, 6 and 2 spectroscopically confirmed multiple image systems. Adding to that, in MACS J0949, we identified four multiply imaged systems, without a confirmed spectroscopic redshift – the spectroscopic emission line not fitting spectral templates convincingly enough, or the images being out of the *VLT/MUSE* field of view. The imaging data, calibrated with the spectroscopic detections of cluster members, allowed to establish conservative cluster galaxy catalogues of respectively 58 and 170 galaxies for MACS J0242 and MACS J0949. We then established the strong lensing mass models of both galaxy clusters. We modelled each individual galaxy with a dPIE profile and included for each cluster a dPIE cluster-scale halo. We present our main results as follows:

(i) The rms on the multiple image positions for the best-fit models are respectively of 0.39 arcsec and 0.15 arcsec, which is considered as a good-quality indicator of the reconstruction. We found that adding a shear-field does not improve the quality of the reconstruction. We note that degeneracies between the BCG and the dark matter halo could hinder the lens model optimizations, and could thus affect our conclusion regarding the morphology of the dark matter distribution in these clusters (see e.g. Limousin et al. 2016).

(ii) Using *XMM–Newton* X-ray observations from CHEX-MATE Collaboration et al. (2021), processed with the X-COP pipeline Ghirardini et al. (2019), we compare the ICM to the reconstructed dark matter density. The combination of the lensing mass reconstructions with the X-ray analyses of the ICM and the *VLT/MUSE* spectroscopy shows that MACS J0242 is in a cool-core, relaxed dynamical state, compatible with a NFW profile, whereas MACS J0949 has a flat distribution between radii of 50 to 100 kpc because it is still undergoing the relaxing process, being in a post-merger dynamical state. In particular, the hot gas fractions at 200 kpc of MACS J0242 and MACS J0949 are $f_{g,200\text{kpc}} = 0.115^{+0.003}_{-0.004}$ and $0.053^{+0.007}_{-0.006}$, respectively. We can for instance compare these results to those of Bonamigo et al. (2018). In Fig. 6, the authors present the cumulative hot gas fraction of each of the three clusters analysed. MACS J0416 is presented as a merging cluster, whereas MACS J1206 and Abell S1063 (RXC J2248) show a cool-core. These clusters have $f_{g,200\text{kpc}} \simeq 0.09$, 0.11 and 0.13, respectively, thus exhibiting the trend of more relaxed clusters displaying higher hot gas fraction values at 200 kpc. This is an additional indication of the relaxed dynamical state of MACS J0242 and the post-merger state of MACS J0949.

(iii) Converting the cluster member catalogue magnitudes into K-band luminosities, we used the Arnouts et al. (2007) mass-to-light ratio relationship to extrapolate the stellar mass detected in both clusters. SED fitting should be performed to obtain a more precise measurement, but this is beyond the scope of this paper. We com-

pare the obtained stellar masses of $M_{\star} = (6.48 \pm 0.62) \times 10^{12} M_{\odot}$ and $(1.39 \pm 0.14) \times 10^{13} M_{\odot}$ for MACS J0242 and MACS J0949, respectively, to the predictions of Giodini et al. (2009), yielding respectively $(8.33 \pm 1.13) \times 10^{12} M_{\odot}$ and $(1.37 \pm 0.30) \times 10^{13} M_{\odot}$. Although not identical in the case of MACS J0242, this means our stellar mass estimates appear to be reasonable.

(iv) We fit the *XMM–Newton* observations to a NFW profile. Projecting this reconstruction, we can measure $M_{2D}(< 200\text{kpc})$, allowing for a direct comparison with the strong lensing model mass estimates. For MACS J0242, we measure $M_{2D}(< 200\text{kpc}) = (1.16 \pm 0.04) \times 10^{14} M_{\odot}$ from the X-rays, to be compared to $1.67^{+0.03}_{-0.05} \times 10^{14} M_{\odot}$ obtained from our strong lensing analysis. We obtain a sizeable 12.75σ difference between these two values. Discrepancies between the X-ray hydrostatic and lensing masses are common and may be explained by the hydrostatic hypothesis bias, or by the presence of asymmetric structures along the line-of-sight. In the former case, the gas is not perfectly relaxed and the thermal pressure only accounts for a fraction of the gravitational pressure. Thus, the hydrostatic mass would underestimate the true mass. Moreover, if there is a distribution of substructures or an elongation of the dark matter component along the line-of-sight, the projected lensing mass may overestimate the 3D mass. For instance, Umetsu et al. (2015) display a combination of both these scenarios.

(v) As for MACS J0949, we measure $M_{2D}(< 200\text{kpc}) = (1.64 \pm 0.07) \times 10^{14} M_{\odot}$ with the X-rays, to be compared with $2.00^{+0.05}_{-0.20} \times 10^{14} M_{\odot}$ obtained with the strong lensing analysis. These values differ by 3.85σ . The *LENSTOOL* and *GLAFIC RELICS* strong lensing models provide $M(R < 200\text{kpc}) = 1.84^{+0.03}_{-0.03} \times 10^{14} M_{\odot}$ and $M(R < 200\text{kpc}) = 1.85^{+0.08}_{-0.07} \times 10^{14} M_{\odot}$, respectively, in good agreement with our model. At last, we compare this latter value to the one obtained with the *Planck* SZ data of $M_{2D}(< 200\text{kpc}) = 1.59^{+0.38}_{-0.00} \times 10^{14} M_{\odot}$ (see Fox et al. 2022), assuming a NFW profile. This 1.49σ difference with the strong lensing value outlines a good agreement with our model.

In order to compare cylindrical masses, we define $R_{10\%} = 0.1R_{200,c}$. For MACS J0242, with $R_{10\%} = 170.2^{+0.39}_{-0.45}$ kpc, we obtain $M_{2D}(< R_{10\%}) = (1.41 \pm 0.03) \times 10^{14} M_{\odot}$ with our strong lensing analysis (for which M_{200} is extrapolated). With $R_{10\%} = 143.0^{+2.7}_{-2.6}$ kpc, we get $M_{2D}(< R_{10\%}) = (8.06 \pm 0.21) \times 10^{13} M_{\odot}$ with the X-rays NFW inferred profile, yielding ratios of $M_{2D}(< R_{10\%})/M_{200,c} = 0.181 \pm 0.014$ and 0.186 ± 0.012 , respectively. This allows us to characterize the ratios of masses measured in the centre and in the outskirts as quite close for X-ray and lensing, in spite of the remarkable difference between the mass measurements. As the strong lensing inferred M_{200} mass obtained here is an extrapolation at larger radii of a profile based on gravitational lensing occurring at $R < 200\text{kpc}$, we cannot claim the strong lensing ratios to be firmly established. Nonetheless, the extrapolated lensing distribution appears to follow a profile similar to that of the X-rays, at different masses. We can compare this result to the ratios found by Bonamigo et al. (2018) for three clusters exhibiting varied dynamical states (Abell S1063, MACS J0416, and MACS J1206), all around 0.13. Let us notice this study uses three to four potentials across all clusters, and thus our models should be expected to yield larger ratios of core-to-outskirts densities. Moreover, as this comparison uses M_{200} values from weak-lensing shear-and-magnification analyses (see Umetsu et al. 2014), we can only cautiously compare it to our X-rays and extrapolated strong lensing measurements. As the ratio is much higher for MACS J0242, this comparison is one more indication that the concentration of mass in the centre of MACS J0242 is particularly high relative to its total mass. This is in good agreement with our

conclusion of the cluster being in a cool-core, relaxed dynamical state.

In the case of MACSJ0949, the cylindrical mass at $R_{10\%} = 205.6_{-25.4}^{+0.00}$ is $M_{2D}(< R_{10\%}) = (2.07 \pm 0.14) \times 10^{14} M_{\odot}$ using our strong lensing measurements and with $R_{10\%} = 184.9_{-11.6}^{+12.6}$, $M_{2D}(< R_{10\%}) = (1.48 \pm 0.05) \times 10^{14} M_{\odot}$ with the X-rays NFW inferred profile. The respective ratios are 0.140 ± 0.025 and 0.146 ± 0.029 . For this cluster again, we notice these ratios to be quite close to one another, supporting the quality of the strong lensing M_{Δ} extrapolation in spite of the large difference between the X-rays and strong lensing measured masses. Interestingly, the comparison with the 0.13 ratio from Bonamigo et al. (2018) hints towards a relative concentration of mass slightly more important in MACSJ0949.

As we have established through strong lensing models the total matter density distribution in two galaxy clusters, we laid the foundations of our companion paper (Allingham et al. in prep.). In this forthcoming paper, we describe a new method using analytical models of galaxy cluster potentials to predict the ICM distribution and in the foreseeable future to put constraints on interacting dark matter.

ACKNOWLEDGEMENTS

JA would like to thank Markus Mosbech for comments and discussions. JA is supported by the International Postgraduate Research Scholarship in Astroparticle Physics/Cosmology at the University of Sydney. MJ and DJL are supported by the United Kingdom Research and Innovation (UKRI) Future Leaders Fellowship ‘Using Cosmic Beasts to Uncover the Nature of Dark Matter’ (grant number MR/S017216/1). DJL is partially supported by ST/T000244/1 and ST/W002612/1. The authors acknowledge the Sydney Informatics Hub and the use of the University of Sydney high performance computing cluster, Artemis. This work is based on observations taken by the RELICS Treasury Program (GO 14096) with the NASA/ESA HST, which is operated by the Association of Universities for Research in Astronomy, Inc., under NASA contract NAS5-26555. GM acknowledges funding from the European Union’s Horizon 2020 research and innovation programme under the Marie Skłodowska-Curie grant agreement No MARACHAS–DLV-896778. ACE acknowledges support from STFC grant ST/P00541/1.

DATA AVAILABILITY

The galaxy and spectroscopic detections catalogues and the lens models are available upon reasonable request to the corresponding author.

REFERENCES

Abbott T. M. C. et al., 2018, *ApJS*, 239, 18
 Ade P. A. R. et al., 2016, *A&A*, 594, A13
 Arnouts S. et al., 2007, *A&A*, 476, 137
 Bacon R. et al., 2014, *The Messenger*, 157, 13
 Bacon R., Piqueras L., Conseil S., Richard J., Shepherd M., 2016, MPDAF: MUSE Python Data Analysis Framework. Astrophysics Source Code Library (ascl:1611.003)
 Bergamini P. et al., 2019, *A&A*, 631, A130
 Bertin E., Arnouts S., 1996, *A&AS*, 117, 393
 Bonamigo M. et al., 2018, *ApJ*, 864, 98
 Bradač M., Allen S. W., Treu T., Ebeling H., Massey R., Morris R. G., von der Linden A., Applegate D., 2008, *ApJ*, 687, 959
 Bruzual G., Charlot S., 2003, *MNRAS*, 344, 1000
 CHEX-MATE Collaboration et al., 2021, *A&A*, 650, A104
 Caminha G. B. et al., 2017, *A&A*, 607, A93
 Caminha G. B. et al., 2019, *A&A*, 632, A36

Chang C. et al., 2018, *ApJ*, 864, 83
 Clowe D., Gonzalez A., Markevitch M., 2004, *ApJ*, 604, 596
 Coe D. et al., 2019, *ApJ*, 884, 85
 Debattista V. P., Moore B., Quinn T., Kazantzidis S., Maas R., Mayer L., Read J., Stadel J., 2008, *ApJ*, 681, 1076
 Diego J. M., Broadhurst T., Molnar S. M., Lam D., Lim J., 2015a, *MNRAS*, 447, 3130
 Diego J. M., Broadhurst T., Zitrin A., Lam D., Lim J., Ford H. C., Zheng W., 2015b, *MNRAS*, 451, 3920
 Diego J. M., Broadhurst T., Wong J., Silk J., Lim J., Zheng W., Lam D., Ford H., 2016, *MNRAS*, 459, 3447
 Diego J. M. et al., 2018, *MNRAS*, 473, 4279
 Diego J. M. et al., 2020, *ApJ*, 904, 106
 Ebeling H., Edge A. C., Henry J. P., 2001, *ApJ*, 553, 668
 Eckert D., Ettori S., Pointecouteau E., van der Burg R. F. J., Loubser S. I., 2022, *A&A*, 662, A123
 Elíasdóttir Á. et al., 2007, preprint (arXiv:0710.5636)
 Ettori S. et al., 2019, *A&A*, 621, A39
 Faber S. M., Jackson R. E., 1976, *ApJ*, 204, 668
 Ford H. C. et al., 1998, in Bely P. Y., Breckinridge J. B., eds, *Society of Photo-Optical Instrumentation Engineers (SPIE) Conference Series Vol. 3356, Space Telescopes and Instruments V*, p. 234
 Fox C., Mahler G., Sharon K., Remolina González J. D., 2022, *ApJ*, 928, 87
 Ghirardini V., Ettori S., Eckert D., Molendi S., Gastaldello F., Pointecouteau E., Hurier G., Bourdin H., 2018, *A&A*, 614, A7
 Ghirardini V. et al., 2019, *A&A*, 621, A41
 Giodini S. et al., 2009, *ApJ*, 703, 982
 Gladders M. D., Yee H. K. C., 2000, *AJ*, 120, 2148
 Grillo C. et al., 2015, *ApJ*, 800, 38
 Grillo C. et al., 2016, *ApJ*, 822, 78
 HI4PI Collaboration et al., 2016, *A&A*, 594, A116
 Hammer F., 1987, in Bergeron J., Kunth D., Rocca-Volmerange B., Tran Thanh Van J., eds, *High Redshift and Primeval Galaxies*, p. 467
 Harvey D., Massey R., Kitching T., Taylor A., Tittle E., 2015, *Science*, 347, 1462
 Hinton S., Davis T. M., Lidman C., Glazebrook K., Lewis G., 2016, *Astron. Comput.*, 15, 61
 Hogg D. W., Baldry I. K., Blanton M. R., Eisenstein D. J., 2002, preprint(astro-ph/0210394)
 Holtzman J. A., Burrows C. J., Casertano S., Hester J. J., Trauger J. T., Watson A. M., Worthey G., 1995, *PASP*, 107, 1065
 Ilbert O. et al., 2010, *ApJ*, 709, 644
 Jauzac M. et al., 2014, *MNRAS*, 446, 4132
 Jauzac M. et al., 2016a, *MNRAS*, 457, 2029
 Jauzac M. et al., 2016b, *MNRAS*, 463, 3876
 Jauzac M. et al., 2016c, *MNRAS*, 463, 3876
 Jauzac M., Harvey D., Massey R., 2018, *MNRAS*, 477, 4046
 Jauzac M. et al., 2019, *MNRAS*, 483, 3082
 Jauzac M., Klein B., Kneib J.-P., Richard J., Rexroth M., Schäfer C., Verdier A., 2021, *MNRAS*, 508, 1206
 Johnson T. L., Sharon K., 2016, *ApJ*, 832, 82
 Jullo E., Kneib J. P., Limousin M., Elíasdóttir Á., Marshall P. J., Verdugo T., 2007, *New J. Phys.*, 9, 447
 Kalirai J., MacKenty J., Bohlin R., Baggett S., Deustua S., Kimble R., Riess A., Sabbi E., 2009, *Space Telescope WFC Instrum. Sci. Rep.*
 Kassiola A., Kovner I., 1993, *ApJ*, 417, 450
 Kneib J.-P., Natarajan P., 2011, *A&A Rev.*, 19
 Kneib J. P., Ellis R. S., Smail I., Couch W. J., Sharples R. M., 1996, *ApJ*, 471, 643
 Lagattuta D. J. et al., 2017, *MNRAS*, 469, 3946
 Lagattuta D. J. et al., 2019, *MNRAS*, 485, 3738
 Lau E. T., Nagai D., Kravtsov A. V., Vikhlinin A., Zentner A. R., 2012, *ApJ*, 755, 116
 Lee J., Suto Y., 2003, *ApJ*, 585, 151
 Limousin M. et al., 2016, *A&A*, 588, A99
 Lin Y.-T., Mohr J. J., Gonzalez A. H., Stanford S. A., 2006, *ApJ*, 650, L99
 Lotz J. M. et al., 2017, *ApJ*, 837, 97
 Lovisari L. et al., 2020, *ApJ*, 892, 102
 Mahler G. et al., 2017, *MNRAS*, 473, 663

Massey R., Kitching T., Nagai D., 2011, *MNRAS*, 413, 1709
 Massey R. et al., 2015, *MNRAS*, 449, 3393
 Massey R. et al., 2018, *MNRAS*, 477, 669
 Mazzotta P., Rasia E., Moscardini L., Tormen G., 2004, *MNRAS*, 354, 10
 Merten J. et al., 2011, *MNRAS*, 417, 333
 Navarro J. F., Frenk C. S., White S. D. M., 1996, *ApJ*, 462, 563
 Newman A. B., Treu T., Ellis R. S., Sand D. J., Nipoti C., Richard J., Jullo E., 2013a, *ApJ*, 765, 24
 Newman A. B., Treu T., Ellis R. S., Sand D. J., 2013b, *ApJ*, 765, 25
 Oguri M., 2010, glafic: Software Package for Analyzing Gravitational Lensing, Astrophysics Source Code Library. preprint(asc1:1010.012)
 Oke J. B., 1974, *ApJS*, 27, 21
 Piqueras L., Conseil S., Shepherd M., Bacon R., Leclercq F., Richard J., 2017, MPDAF-A Python package for the analysis of VLT/MUSE data. preprint (arXiv:1710.03554)
 Postman M. et al., 2012, *ApJS*, 199, 25
 Richard J. et al., 2014a, *MNRAS*, 444, 268
 Richard J. et al., 2014b, *MNRAS*, 444, 268
 Richard J. et al., 2021, *A&A*, 646, A83
 Robertson A., Massey R., Eke V., 2016, *MNRAS*, 465, 569
 Robertson A., Massey R., Eke V., 2017, *MNRAS*, 467, 4719
 Schneider P., Ehlers J., Falco E. E., 1992, in *Gravitational Lenses*. Springer, Berlin, Heidelberg
 Sereno M., Ettori S., Meneghetti M., Sayers J., Umetsu K., Merten J., Chiu I.-N., Zitrin A., 2017, *MNRAS*, 467, 3801
 Sharon K. et al., 2020, *ApJS*, 247, 12
 Smith R. K., Brickhouse N. S., Liedahl D. A., Raymond J. C., 2001, *ApJ*, 556, L91
 Soucail G., Mellier Y., Fort B., Mathez G., Cailloux M., 1988, *A&A*, 191, L19
 Stapelberg S., Tchernin C., Hug D., Lau E. T., Bartelmann M., 2022, *A&A*, 663, A17
 Steinhardt C. L. et al., 2020, *ApJS*, 247, 64
 Tchernin C. et al., 2018, *A&A*, 614, A38
 Treu T. et al., 2016, *ApJ*, 817, 60
 Trevisan M., Mamon G. A., 2017, *MNRAS*, 471, 2022
 Tulin S., Yu H.-B., 2018, *Phys. Rep.*, 730, 1
 Umetsu K. et al., 2014, *ApJ*, 795, 163
 Umetsu K. et al., 2015, *ApJ*, 806, 207
 Umetsu K. et al., 2018, *ApJ*, 860, 104
 Williams L. L. R., Sebesta K., Liesenborgs J., 2018, *MNRAS*, 480, 3140

APPENDIX A: SPECTROSCOPIC DETECTIONS OF INTEREST

We present additional spectroscopic good detections in the background of both clusters MACS J0242 and MACS J0949, respectively, in Tables A1 and A2.

Table A1. Spectroscopic detections of singly imaged objects in MACS J0242. Coordinates are in degrees (J2000). The reference for right ascension and declination are taken to be the centre of the cluster.

Id.	R.A.	Dec.	z
10	40.6559072	−21.5412424	0.5756
11	40.6536287	−21.5327925	0.5928
12	40.6546722	−21.5328188	0.5937
13	40.6466813	−21.5480705	0.5942
14	40.6517158	−21.5453613	0.5943
15	40.6566147	−21.5399484	0.5943
16	40.6552620	−21.5388619	0.7707
17	40.6551537	−21.5382257	0.7713
18	40.6407123	−21.5444971	0.8363
19	40.6508138	−21.5463873	0.8380
20	40.6457745	−21.5366071	3.1120

Table A2. Spectroscopic detections of singly imaged objects images in MACS J0949. Coordinates are in degrees (J2000). The reference for R.A. and declination are taken to be the centre of the cluster.

Id.	R.A.	Dec.	z
10	147.46989360	17.11231290	0.5841
11	147.46892360	17.12212680	0.6395
12	147.45946988	17.11584094	0.8472
13	147.46832980	17.11256280	0.8473
14	147.46913850	17.12435220	0.8488

Table A3. The brightest cluster members in the cluster MACS J0242. Coordinates are in degrees (J2000). We remind that the reference coordinates are (40.649555; −21.540485) deg. Magnitudes are given on the reference band ACS/F606W. All spectroscopic redshift detections are also provided.

Id.	Δ_α	Δ_δ	a	b	θ	Mag.	z
1	0.04387	−0.08964	1.886	1.499	1.83	17.765	0.3130
2	−31.28771	72.89640	1.027	0.396	2.34	19.898	−
3	59.25290	79.37028	0.595	0.593	−14.20	20.055	−
4	82.31906	−5.37408	0.829	0.501	23.90	20.081	−
5	−47.40417	−5.82480	0.731	0.410	−4.47	20.214	−

Table A4. Brightest cluster members in the MACS J0949. Coordinates are in degrees (J2000). We remind that the reference coordinates are (α_c, δ_c) = (147.4659012, 17.1195939). Magnitudes are given on the reference band ACS/F814W.

Id.	Δ_α	Δ_δ	a	b	θ	Mag.	z
1	−51.61743	−32.11128	1.344	0.709	45.31	18.761	−
2	0.05608	−0.15120	1.344	0.740	−57.20	18.789	0.3829
3	−17.02960	5.76108	0.704	0.657	60.72	18.875	0.3817
4	51.33490	121.06692	0.742	0.529	50.52	18.970	−
5	15.93092	−74.92248	0.812	0.526	−24.40	19.054	−

We present in Tables A3 and A4 (respectively for clusters MACS J0242 and MACS J0949) a few cluster members in their final catalogue format: their positions and all geometrical components (semimajor and minor axes a and b , rotation angle θ) as well as their magnitudes are coming from the photometric analysis, whereas the redshifts are detected through spectroscopy.

APPENDIX B: ADDITIONAL INFORMATION ON COLOUR-MAGNITUDE DIAGRAMS SELECTIONS

We here provide the equation of each main red colour sequence for both galaxy cluster MACS J0242 and MACS J0949, according to process described in Section 3.2.3. We also provide all the additional colour-magnitude diagrams we can plot. Tables B1 and B2 provide, respectively, the equations of the main colour sequences of clusters MACS J0242 and MACS J0949 and the weighed colour standard deviation of the spectroscopically confirmed cluster galaxy sample σ_C . The height of the selection box is $2\sigma_C$ away from the main red sequence for *HST*/ACS and *HST*/WFC3, and $3\sigma_C$ for *HST*/WFPC2 and DES.

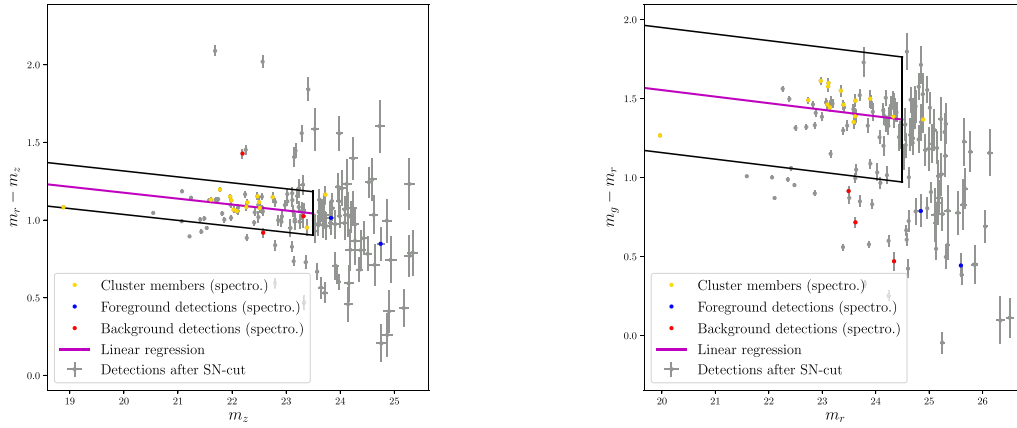


Figure B1. Colour-magnitude diagram for MACS J0242, instrument DES. Top row: Left: The colour is $(m_r - m_z)$, and the magnitude m_z . Right: m_z versus $(m_g - m_r)$. Grey filled circles (with their error bars) have successfully passed all selections described in Section 3.2.1. The magenta line represents the main sequence regression. Blue, gold, and red dots represent spectroscopic detections of foreground, cluster, and background objects, respectively.

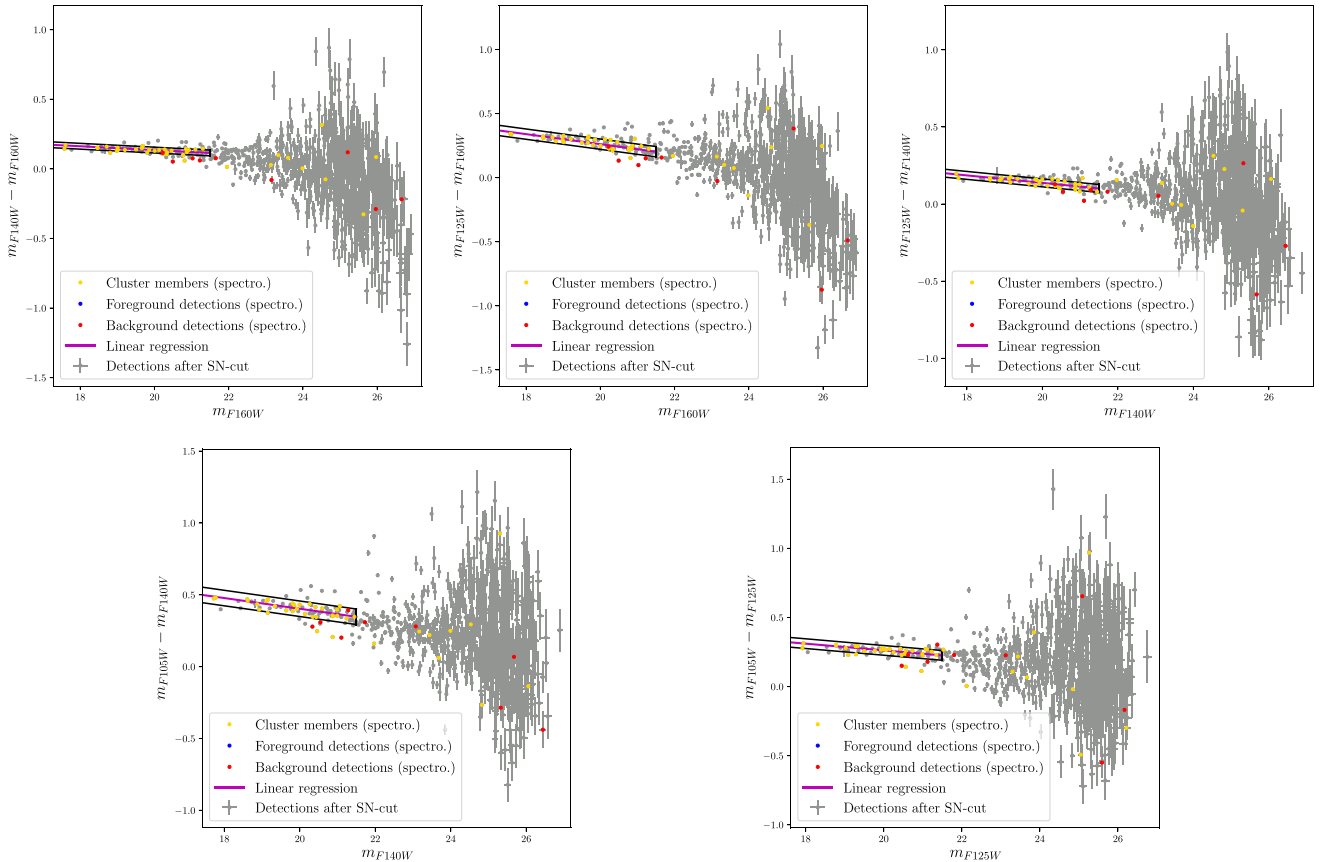


Figure B2. Colour-magnitude diagrams for cluster MACS J0949, instrument *HST*/WFC3. Top row: Left: The colour is $(m_{F140W} - m_{F160W})$, and the magnitude m_{F160W} . Middle: m_{F160W} versus $(m_{F125W} - m_{F160W})$. Right: m_{F140W} versus $(m_{F105W} - m_{F140W})$. Bottom row: Left: m_{F140W} versus $(m_{F105W} - m_{F140W})$. Right: m_{F125W} versus $(m_{F105W} - m_{F125W})$. Grey filled circles (with their error bars) have successfully passed all selections described in Section 3.2.1. The magenta line represents the main sequence regression. Blue, gold, and red dots represent spectroscopic detections of foreground, cluster, and background objects, respectively.

Table B1. Equations of the main colour sequences and standard deviations on colours for all colour-magnitude diagrams of MACS J0242. m_1 represents the magnitude in abscissa. Associated graphs are Fig. 4 and B1.

Filter 1	Filter 2	σ_C	Main colour sequence equation
<i>HST/WFPC2</i>			
F814W	F606W	0.0508	$-0.0307m_1 + 1.6176$
DES			
z	r	0.0466	$-0.0382m_1 + 2.078$
z	g	0.1651	$-0.0744m_1 + 4.651$
r	g	0.1319	$-0.0415m_1 + 2.779$

Table B2. Equations of the main colour sequences and standard deviations on colours for all colour-magnitude diagrams of MACS J0949. m_1 represents the magnitude in abscissa. Associated graphs are Fig. 4 and B2.

Filter 1	Filter 2	σ_C	Main colour sequence equation
<i>HST/ACS</i>			
F814W	F606W	0.1956	$-0.0317m_1 + 2.0530$
<i>HST/WFC3</i>			
F160W	F140W	0.0230	$-0.0121m_1 + 0.4217$
F160W	F125W	0.0365	$-0.0253m_1 + 0.8511$
F160W	F105W	0.0684	$-0.0483m_1 + 1.6344$
F140W	F125W	0.0220	$-0.0158m_1 + 0.5043$
F140W	F105W	0.0523	$-0.0361m_1 + 1.2308$
F125W	F105W	0.0371	$-0.0209m_1 + 0.7565$

This paper has been typeset from a $\text{\TeX}/\text{\LaTeX}$ file prepared by the author.